Journal of Molecular Liquids 413 (2024) 125743

Contents lists available at ScienceDirect

Journal of Molecular Liquids

journal homepage: www.elsevier.com/locate/molliq

# Atranorin is a novel potential candidate drug for treating myelodysplastic syndrome

Konstantin N. Semenov [a,b,*], Ilya A. Prokopiev [c], Natalya V. Petukhova [a], Uliana A. Kremenetskaya [b], Dina A. Senichkina [a], Olga S. Epifanovskaya [a], Andrei M. Rumiantsev [b], Pavel A. Andoskin [a], Jasur A. Rizaev [d], Dilafruz K. Kholmurodova [d], Sergei V. Ageev [a,b], Yurii A. Anufrikov [b], Egor E. Zakharov [a], Ivan S. Moiseev [a], Vladimir V. Sharoyko [a,b,*]

[a] Pavlov First Saint Petersburg State Medical University, 6–8 L'va Tolstogo Street, Saint Petersburg 197022, Russia
[b] Saint Petersburg State University, 7–9 Universitetskaya Embankment, Saint Petersburg, 199034, Russia
[c] Komarov Botanical Institute of the Russian Academy of Sciences, 2 Professor Popov Street, Saint Petersburg, 197376, Russia
[d] Samarkand State Medical University, 18 Amir Temur Street, Samarkand, 140100, Uzbekistan

ARTICLE INFO

*Keywords:*
Atranorin
Biocompatibility
Cytotoxicity
Genotoxicity
AKT kinase
Flow cytometry

ABSTRACT

This work is devoted to the study of biocompatibility, cyto- and genotoxicity, mechanism of action and prospects for the use of atranorin, which is an AKT kinase inhibitor, for the treatment of myelodysplastic syndrome. Atranorin was isolated by preparative flash chromatography; identification was carried out by UV, IR, and NMR spectroscopy, mass spectrometry, and elemental analysis. Biocompatibility studies included studies of haemocompatibility, genotoxicity, antioxidant activity, cytotoxicity against ECV340 and HEK293 cell lines. Computer modelling of the interaction of atranorin with AKT kinase was carried out using docking followed by molecular dynamics of the resulting complexes; the ADMET properties of atranorin were also calculated. Flow cytometry included analysis of the expression level of PD-L1 and TIM-3 in the presence of atranorin on THP-1, Mono-Mac-1 and KG-1 cell lines, as well as human bone marrow cells.

## 1. Introduction

Lichens are producers of a large number of specific secondary metabolites, most of which are not found in other living organisms [1,2]. Currently, more than 800 secondary metabolites of lichens are known [1]. The majority of aromatic lichen metabolites (about 500 compounds) are formed during the acetate-polymalonate biosynthetic pathway, which occurs with the participation of polyketide synthase (PKS) enzymes, which are very similar to fatty acid synthases in the organisation and mechanism of biosynthesis [1].

The most numerous classes of lichen metabolites formed along the acetate-polymalonate biosynthetic pathway are depsides and depsidones, which are formed by combining two or less often three phenolic rings of the orsinol or β-orsinol type through ether and ester bonds [3]. It is believed that the additional methyl group at C-3 in β-orsinol type rings is added to the tetraketide before cyclisation with the participation of PKS [1]. Phenolic rings of the β-orsinol type most often differ in the degree of oxidation of the alkyl substituents in both the sixth and third positions [2,3].

Atranorin (Fig. 1) belongs to the β-orsinol type depsides and is often the main metabolite in many lichen families *Cladoniaceae*, *Parmeliaceae*, *Streocaulaceae* and others [2]. The compound was first isolated by O. Hesse in 1898 and since then its properties, pharmacological and biological activities have been intensively studied. The antibacterial properties of atranorin began to be studied in the middle of the 20th century. One of the first published studies showed weak activity of this depside against mycobacterium tuberculosis and staphylococci [4]. The antibacterial activity of atranorin against strains of gram-positive and gram-negative bacteria has been studied by various authors [5]. Although atranorin exhibited pronounced bactericidal properties against *Staphylococcus aureus*, *Escherichia coli* and *Klebsiella pneumoniae*, its activity was lower than that of such antibiotics as streptomycin, levofloxacin, erythromycin and gentamicin [6,7].

Studies of the antiviral activity of atranorin against hepatitis C virus

* Corresponding authors at: 6–8 L'va Tolstogo Str., Saint Petersburg, 197022, Russia.
*E-mail addresses:* semenov1986@yandex.ru, knsemenov@gmail.com (K.N. Semenov), sharoyko@gmail.com (V.V. Sharoyko).

https://doi.org/10.1016/j.molliq.2024.125743
Received 5 July 2024; Received in revised form 2 August 2024; Accepted 10 August 2024
Available online 11 August 2024

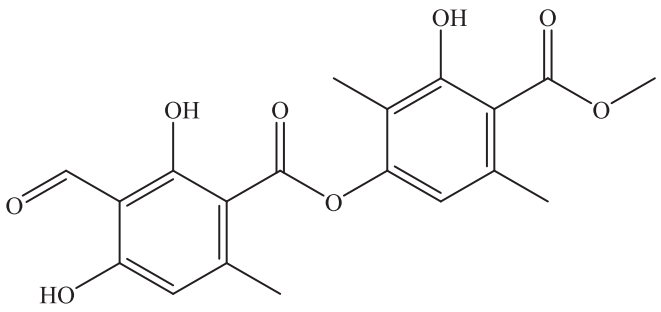


**Fig. 1.** Structural formula of atranorin.

**Table 1**
Characteristics of atranorin obtained by HPLC and electrospray time-of-flight mass spectrometry. M — atranorin ($C_{19}H_{18}O_8$). $t_R$ is retention time.

| Analyte | $t_R$/min | Molecular formula | Ion $[M-H]^-/m/z$ | Δ/ppm* |
|---|---|---|---|---|
| Atranorin | 31.6 | $C_{19}H_{18}O_8$ | 373.0929 | 0.03 |

* Discrepancy between calculated and observed ion masses.

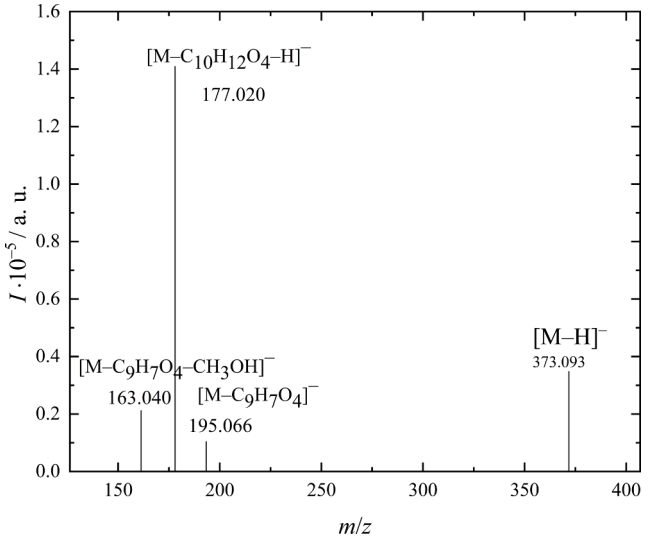


**Fig. 2.** Mass spectrum of atranorin with electrospray ionisation in the detection mode of negative ions. M are molecular ions of atranorin ($C_{19}H_{18}O_8$).

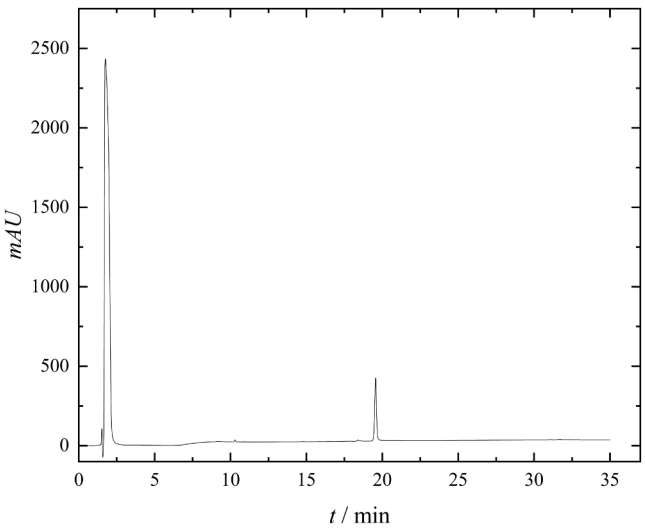


**Fig. 3.** Chromatogram of atranorin obtained by HPLC in a mixture of 0.1 % aqueous solution of formic acid and acetonitrile in a gradient elution mode.

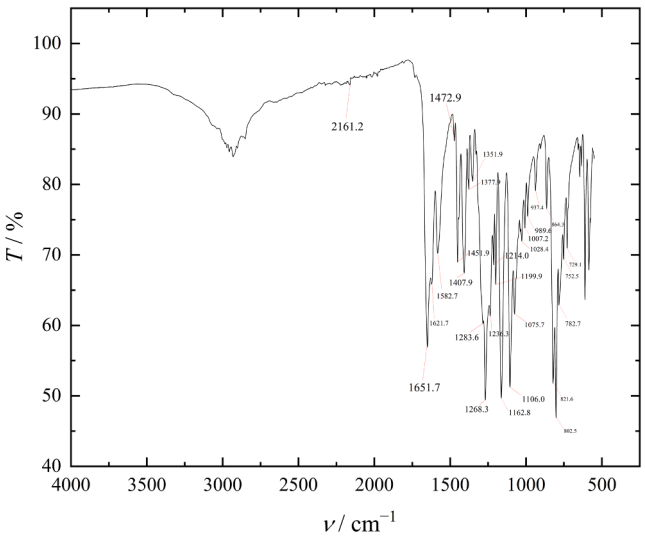


**Fig. 4.** IR spectrum of atranorin.

(HCV) showed that depside is active against HCV with an $IC_{50}$ of 22.3 μM, while erlotinib and telaprevir, used as controls, had $IC_{50}$ of 0.64 and 0.18 μM, respectively [8]. Evaluation of the activity of atranorin *in vitro* against the HCoV-229E virus did not reveal a pronounced antiviral effect [9].

The cytotoxic activity of atranorin was studied against a number of tumour and normal cells. In most cases, the effect is described as weak [10–12] or moderate [13,14]. Studies of the cytotoxic activity of atranorin against human melanoma cells (FemX) and human colon cancer (LS 174) showed the following activity: $IC_{50}$ (FemX) = 20.9 μg•ml$^{-1}$ (0.056 μM), and $IC_{50}$ (LS 174) = 24.6 μg•ml$^{-1}$ (0.066 μM) [15]. Cytotoxicity of depside against human lung adenocarcinoma cells (A549) was also revealed: at an atranorin concentration of 25 μg • ml$^{-1}$ (0.067 μM), an 80 % loss of cell viability was observed [16].

Information on the mechanism of cytotoxic activity of atranorin is scarce [13,17–19]. Atranorin has been shown to stimulate apoptosis in both tumour and normal cell lines. A study of the effect of atranorin on caspase-3 activity in normal rat hepatocytes revealed a moderate increase in the activity of the early apoptosis enzyme [13]. At the same time, the results of other studies showed that atranorin does not affect the expression of proteins involved in apoptosis (Bcl-2, Bax, Hsp70, etc.), and also does not increase the activity of caspase-3 [19]. Evaluation of the effect of atranorin on the expression of apoptotic proteins (Bax, caspase-3, 7 and 9) in tumour (melanoma HTB-140, prostate adenocarcinoma DU-145 and PC-3) and normal (human skin fibroblasts HSF and prostate cells PNT-2) cell lines also did not reveal the proapoptotic activity of depsid [17].

Myelodysplastic syndrome accounts for about 1 % of all malignant diseases, but is nevertheless associated with significant mortality. For example, in Europe and the USA, epidemiological assessment of the disease remains challenging due to the development of classification systems, but the overall incidence is about five cases per 100,000 people per year after 60 years of age and increases with age [20–22].

Currently, there are no conservative approaches to treating this disease that led to a cure, so improving the results of treatment of myelodysplastic syndrome will contribute to reducing overall mortality from cancer. Standard treatments for high-risk myelodysplastic syndrome provide about 12 months of additional treatment compared with best supportive care and are not curative in the vast majority of these patients. Today, the development of AKT kinase inhibitors for the

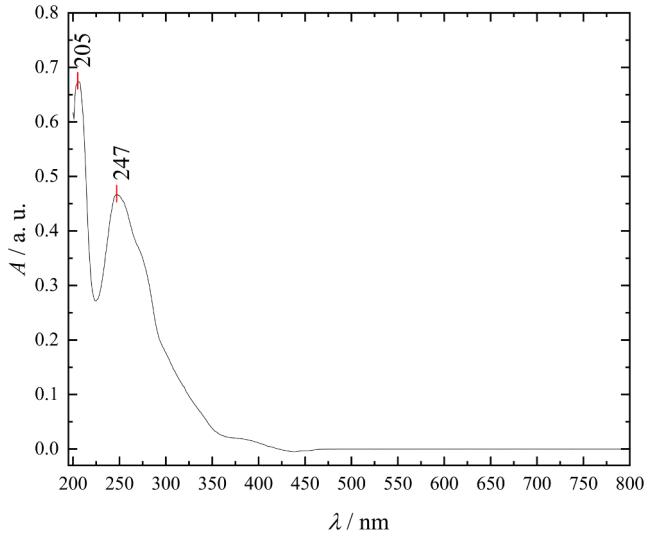


**Fig. 5.** UV/Vis spectrum of a solution of atranorin in methanol ($C$ = 37.5 μM).

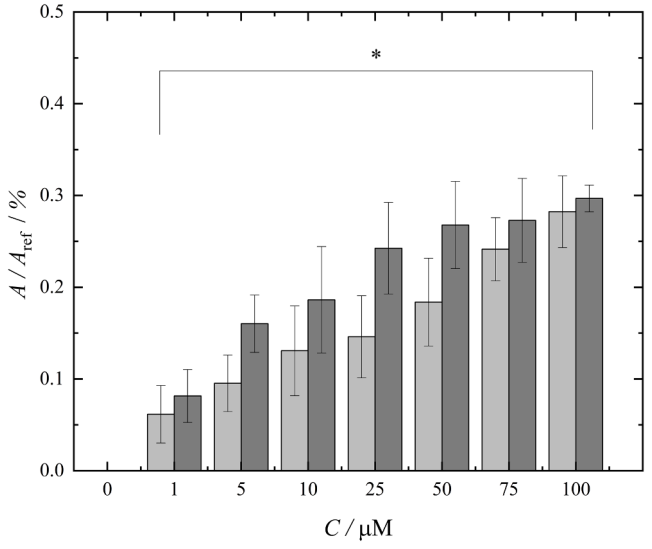


**Fig. 6.** Effect of atranorin on haemolysis after incubation for 1 h (light grey) and 3 h (dark grey). $C$ is the molar concentration of atranorin (*$p$ < 0.05 compared to control).

treatment of myelodysplastic syndrome, which affect the expression of PDL-1 and TIM3 proteins of the 'checkpoint' system, is relevant. The mechanism of suppression of the antitumor immune response by changing the expression of checkpoint molecules is common in many tumour diseases. Atranorin has previously been shown to be an AKT kinase inhibitor [23].

This work presents a method for the isolation and purification of atranorin from the lichen *C. rangiferina* which was collected at the end of July 2021 in a pine forest in Yakutia, Russia (61.923198°N 129.535190°E). Identification of atranorin was carried out using a complex of physicochemical methods of analysis. The biocompatibility study included the study of haemocompatibility, binding to DNA and HSA, the study of cyto- and genotoxicity, as well as antioxidant properties. The effect of atranorin on the expression level of PD-L1 and TIM-3 proteins was studied using flow cytometry. The interaction of atranorin with AKT kinase was demonstrated by molecular docking followed by molecular dynamics of the complexes.

**Table 3**
Values of binding constants ($K_b$) and binding stoichiometry ($n$) of the interaction of atranorin with RatCol at different temperatures.

| $T$/K | $K_b \bullet 10^5/M^{-1}$ | $n$ |
|---|---|---|
| 298.2 | 0.16 ± 0.01 | 0.90 ± 0.03 |
| 302.1 | 0.28 ± 0.01 | 0.95 ± 0.03 |
| 306.2 | 0.42 ± 0.03 | 1.00 ± 0.06 |
| 310.0 | 1.55 ± 0.07 | 1.10 ± 0.05 |
| 314.3 | 9.27 ± 0.18 | 1.38 ± 0.02 |

**Table 4**
Values of changes in enthalpy ($\Delta H$), entropy ($\Delta S$) and Gibbs energy ($\Delta G$) of the binding of atranorin to RatCol.

| $T$ / K | $-\Delta G$/kJ·mol$^{-1}$ | $\Delta H$/kJ·mol$^{-1}$ | $\Delta S$/J·mol$^{-1}$·K$^{-1}$ |
|---|---|---|---|
| 298.2 | 23.1 ± 3.3 | 206 ± 22 | 770 ± 73 |
| 302.1 | 26.1 ± 3.8 | | |
| 306.2 | 29.3 ± 4.2 | | |
| 310.0 | 32.2 ± 4.6 | | |
| 314.3 | 35.5 ± 5.1 | | |

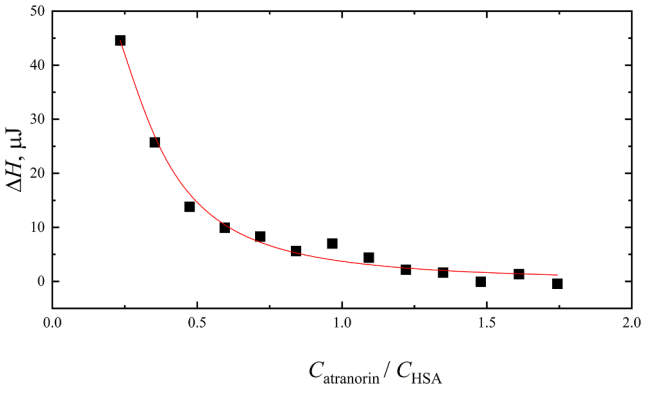


**Fig. 7.** Dependence of the thermal effect of the reaction of interaction of atranorin with HSA at 298.15 K. $\Delta H$ is the thermal effect of the reaction, $C_{atranorin}$ / $C_{HSA}$ is the ratio of the molar concentrations of atranorin and HSA.

**Table 2**
The effect of atranorin on ADP-, collagen- and adrenaline-induced platelet aggregation.

| Inductor | Control | Amplitude/% | | | | | | |
|---|---|---|---|---|---|---|---|---|
| | | $C_{atranorin}$/μM | | | | | | |
| | | 1 | 5 | 10 | 25 | 50 | 75 | 100 |
| ADP | 84.2 ± 0.4 | 85.6 ± 1.6 | 87.7 ± 1.6* | 87.4 ± 1.9* | 91.0 ± 1.05* | 88.2 ± 1.9* | 89.3 ± 1.00* | 87.8 ± 1.8* |
| Collagen | 94.5 ± 1.8 | 97.7 ± 0.2* | 98.5 ± 0.1* | 94.2 ± 2.0* | 98.2 ± 0.4* | 96.1 ± 0.5* | 96.3 ± 0.8* | 98.4 ± 0.3* |
| Adrenaline | 54.8 ± 5.8 | 79.5 ± 0.6* | 78.4 ± 0.9* | 73.7 ± 6.5* | 76.0 ± 3.6* | 71.8 ± 8.3* | 71.2 ± 2.8* | 78.5 ± 5.4* |

* $p$ < 0.05 compared to control.

**Table 5**
Thermodynamic characteristics of atranorin binding to HSA and DNA. $K_d$ is the dissociation constant, $K_b$ is the binding constant, n is the stoichiometric coefficient of binding of atranorin with HSA or DNA, $\Delta H$, $\Delta S$, $\Delta G$ is the change in enthalpy, entropy and Gibbs energy in the reaction of atranorin with HSA or DNA, T is the absolute temperature.

| Thermodynamic parameter | HSA-atranorin | DNA-atranorin |
|---|---|---|
| $K_d$/M | $1.32 \cdot 10^{-5}$ | $3.48 \cdot 10^{-5}$ |
| $n$ | 0.13 | 1.12 |
| $\Delta H$/kJ·mol$^{-1}$ | 18.03 | −1.57 |
| $\Delta S$/J·mol$^{-1}$·K$^{-1}$ | 153.9 | 80.1 |
| $\Delta G$/kJ·mol$^{-1}$ | −27.86 | −25.45 |
| $-T\Delta S$/kJ·mol$^{-1}$ | −45.89 | −23.88 |
| $K_b$/M$^{-1}$ | $7.60 \cdot 10^{4}$ | $2.88 \cdot 10^{4}$ |

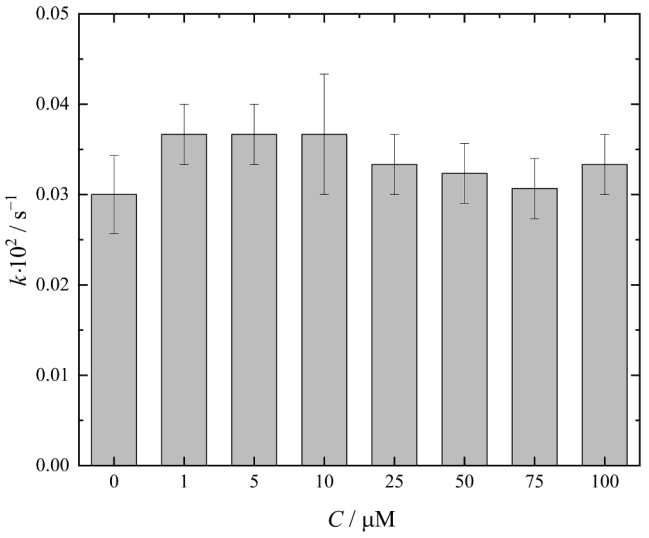


**Fig. 8.** Rate constants for the hydrolysis of NPA under the influence of HSA in the absence and presence of atranorin ($C$ = 50 μM).

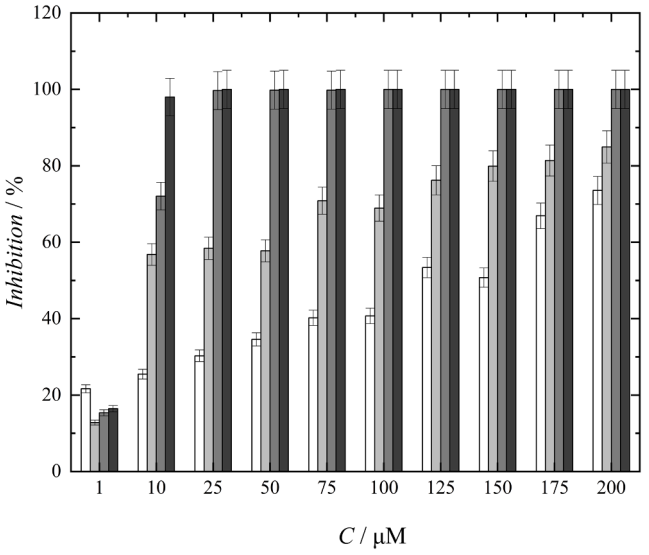


**Fig. 9.** Dependence of the fraction of reduced radicals on the concentration of atranorin and ascorbic acid (for comparison) 30 min after the start of the reaction: □ — atranorin with DPPH; ■ — atranorin with ABTS; ■ — ascorbic acid with DPPH; ■ — ascorbic acid with ABTS.

## 2. Experimental part

### 2.1. Identification of atranorin

Identification of atranorin was carried out using NMR spectroscopy, high-performance liquid chromatography, IR, UV spectroscopy, mass spectrometry, and elemental analysis.

$^1$H (400 MHz), $^{13}$C{$^1$H} NMR spectra were recorded on a Bruker Avance spectrometer (Germany). The NMR spectrum of atranorin in deuterated DMSO is shown in Fig. S1. Analysis of Fig. S1 allows to select the following signals: $^1$H NMR (400 MHz, DMSO) $\delta$ 12.43 (s, 1H, OH), 10.55 (s, 1H, OH), 10.21 (s, 1H, OH), 6.64 (s, 1H, $CH_{Ar}$), 6.44 (s, 1H, $CH_{Ar}$), 3.87 (s, 3H, $CH_3$), 2.39 (s, 3H, $CH_3$), 2.35 (s, 3H, $CH_3$), 2.03 (s, 3H, $CH_3$). $^{13}$C NMR (101 MHz, DMSO) $\delta$ 194.27, 170.21, 165.04, 157.78, 151.83, 149.51, 137.22, 116.64, 116.20, 115.48, 109.43, 108.19, 52.81, 21.58, 9.70.

The isolated atranorin was studied by HPLC in combination with time-of-flight mass spectrometry on an Agilent 6538 UHD (USA) quadrupole time-of-flight (qTOF) mass spectrometer with electrospray ionisation (ESI). The voltage on the capillary with positive and negative ESI was 2.5 kV; capillary temperature was 350 °C; nebuliser gas pressure was 45 psi; temperature of the drying gas (nitrogen) was 225 °C; drying gas flow rate was 5 l min$^{-1}$. Only ions formed during negative ESI without their additional dissociation induced by collisions were recorded in MS/MS mode, in the mass range 100–1000 $m/z$. HPLC and electrospray time-of-flight mass spectrometry data are given in Table 1. As can be seen from Table 1, with negative electrospraying, the formation of molecular ions of atranorin (M) $[M-H]^-$ occurred. Mass spectra of standard samples of the studied atranorin are shown in Fig. 2.

The analytical purity of atranorin was determined on an Agilent 1290 high-performance liquid chromatograph (USA). A mixture of 0.1 % aqueous solution of formic acid and acetonitrile was used as the mobile phase; the analysis was carried out in a gradient elution mode with an increase in the proportion of acetonitrile from 10 to 100 % over 40 min at a flow rate of 300 μl min$^{-1}$ and a column temperature of 30 °C. A ZORBAX SB-C18 reverse-phase column (150 × 2.1 mm, 3.5 μm) was used for separation. The volume of the introduced sample is 5 μl. Detection was carried out at a wavelength of 250 nm. Analysis of the chromatogram of atranorin allows to conclude that the purity of the isolated product is 99.9 % (Fig. 3).

IR spectrum (Fig. 4) of atranorin was recorded in the range of 4000–400 cm$^{-1}$ in potassium bromide tablets on a Varian 7000 FT-IR spectrometer (USA). Analysis Fig. 4 allows to detect the following signals: $\nu$, cm$^{-1}$ (KBr): 2161.2, 1651.7, 1621.7, 1582.7, 1472.9, 1451.9, 1407.9, 1377.9, 1351.9, 1283.6, 1268.3, 1236.3, 1214.0, 1199.9, 1162.8, 1106.0, 1075.7, 1028.4, 1007.2, 989.6, 937.4, 864.3, 821.6, 802.5, 782.7, 752.5, 729.1.

UV spectrum of atranorin was recorded in the range of 200–800 nm on a Beckman Coulter DU 800 spectrophotometer. Fig. 5 shows the spectrum of a solution of atranorin in methanol ($C$=37.5 μM). It can be seen that the electronic spectrum contains absorption band maxima at $\lambda$ = 205 nm and 247 nm.

Elemental analysis of atranorin ($C_{19}H_{18}O_8$) was carried out on a Euro EA 3028 HT CHNSO analyser. Experimental values: 60.9 % (C), H 4.8 % (H). Theoretical content ($C_{19}H_{18}O_8$): 60.9 % (C), 4.8 % (H).

### 2.2. Study of biocompatibility and biological activity

The study with human blood samples (erythrocytes, platelets, peripheral blood mononuclear cells (PBMCs) and nucleated bone marrow cells was approved by the Local Ethics Committee of the Pavlov First Saint Petersburg State Medical University, and the procedures followed were in accordance with University guidelines and ethical standards. An informed consent form was received from the volunteers of 22–32 years old (males, n = 12), which were recruited by the laboratory staff of the Clinical Centre at the Pavlov First Saint Petersburg State Medical

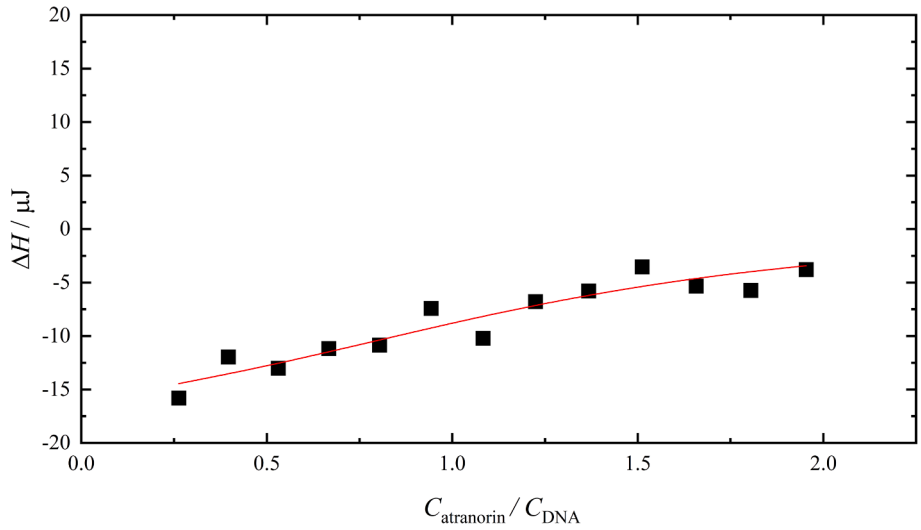


**Fig. 10.** Dependence of the thermal effect of the reaction of interaction of atranorin with DNA at 298.15 K. $\Delta H$ is the thermal effect of the reaction, $C_{atranorin}$ / $C_{DNA}$ is the ratio of the molar concentrations of atranorin and DNA.

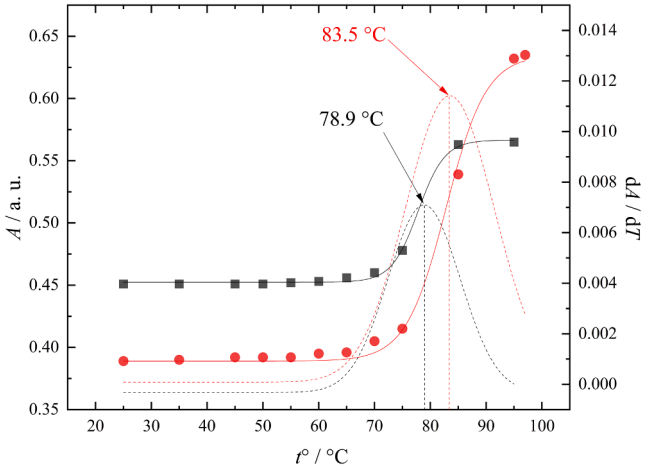


**Fig. 11.** Melting curves of DNA in saline (■) ($C_{DNA}$ = 3.4·10$^{-8}$ M) and DNA complex with atranorin ($C_{atranorin}$ = 1.3·10$^{-5}$ M) (●); dotted lines are differential curves.

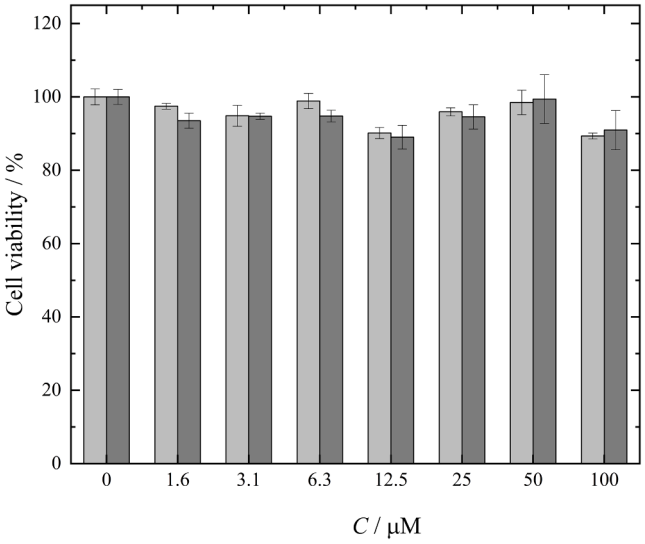


**Fig. 12.** Effect of atranorin on the viability of cell lines ECV340 (light grey) and HEK293 (dark grey). $C$ is the molar concentration of atranorin.

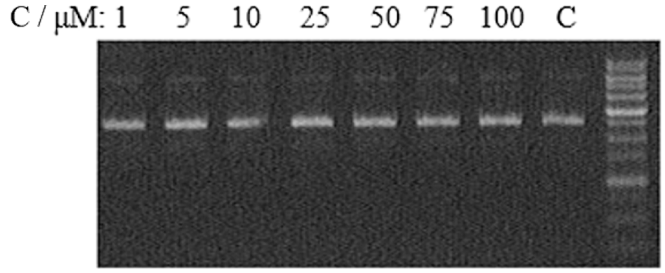


**Fig. 13.** Effect of atranorin on genotoxicity in the model experiment containing pBR322 plasmid. $C$ — control.

University.

The reagents used to study the biocompatibility and biological activity of atranorin are given in Table S1.

The distribution of atranorin in the octan-1-ol–$H_2O$ system was studied using a LAUDA ET 20 shaker-thermostat (Germany, shaking frequency 200 rpm) at a temperature of 298.15 K for 5 h. A solution of atranorin ($C$=0.013 g l$^{-1}$) was prepared for the experiment) in deionised water, to which an equal volume of octan-1-ol (5 ml) was added. The optical density of the atranorin solution in the aqueous phase was measured on an SF-2000 spectrophotometer (Russia) at a wavelength of 250 nm. Details of the experimental procedure are described in [24]. A total of 5 parallel measurements were made.

The effect of atranorin on spontaneous haemolysis was studied by measuring the optical density of the supernatants at a wavelength of $\lambda$ = 540 on an Allsheng AMR-100 microplate reader photometer (China) according to a previously described method 25. The concentration range of atranorin was 1–100 μM.

To study platelet aggregation, blood was collected into vacuum tubes containing sodium citrate ($C$=0.129 M) as a stabiliser at a sodium citrate: blood ratio of 1:9 (v/v). Platelet aggregation in platelet-rich plasma (PRP) was studied in the presence of aggregation inducers ADP ($C$=0.005 g·l$^{-1}$), collagen ($C$=20 g l$^{-1}$) and adrenaline ($C$=0.005 g·l$^{-1}$) [25].

A study of the binding of atranorin to collagen isolated from rat tails (RatCol) was carried out using a Solar CM2203 spectrofluorimeter (Belarus). Emission spectra were recorded in the wavelength range

**Table 6**
Effect of atranorin on the percentage of DNA in a comet's tail, tail length, and tail moment of comets.

| Characteristic | Amplitude/% | | | | | | | | |
|---|---|---|---|---|---|---|---|---|---|
| | Negative control (PBS) | $C(H_2O_2)$/μM | $C_{atranorin}$/μM | | | | | | |
| | 0 | 100.0 | 1.0 | 5.0 | 10.0 | 25.0 | 50.0 | 75.0 | 100.0 |
| Tail DNA, % | 16.93 ± 3.24 | 83.12 ± 10.14 | 14.54 ± 5.10 | 17.34 ± 6.15 | 15.84 ± 4.43 | 16.67 ± 3.96 | 15.29 ± 5.11 | 18.34 ± 6.30 | 16.93 ± 8.17 |
| Tail length, μm | 69.25 ± 14.15 | 522.56 ± 55.81 | 64.22 ± 12.28 | 81.99 ± 16.81 | 71.73 ± 10.73 | 80.15 ± 9.17 | 70.61 ± 5.72 | 111.72 ± 21.19 | 74.81 ± 11.20 |
| Tail moment | 11.72 ± 0.45 | 434.35 ± 5.66 | 9.34 ± 0.63 | 14.22 ± 1.03 | 11.36 ± 0.48 | 13.36 ± 0.36 | 10.80 ± 0.29 | 20.49 ± 1.33 | 12.66 ± 0.92 |

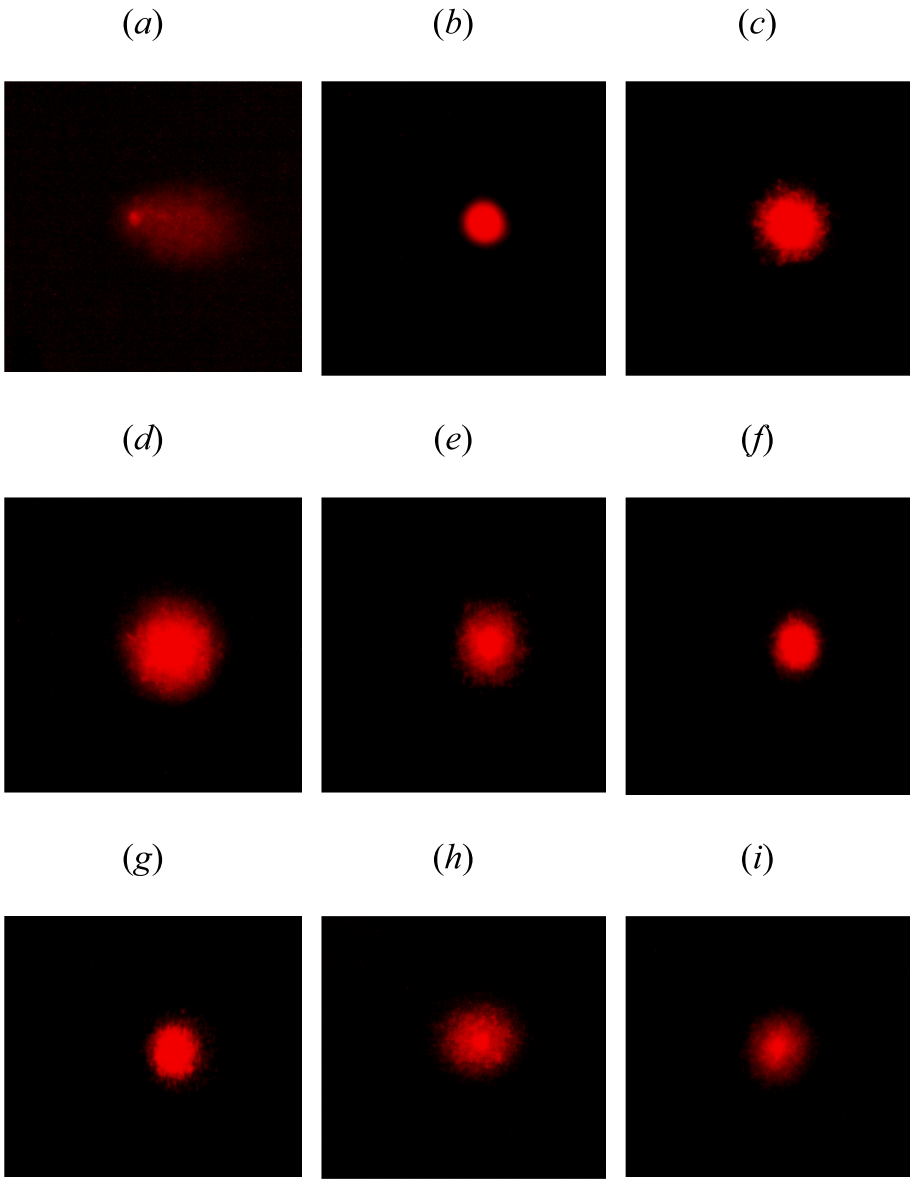


**Fig. 14.** DNA comets after electrophoresis of PBMCs in a microgel: (*a*) — positive control ($H_2O_2$), (*b*) — negative control (PBS), (*c–i*) — atranorin ($C$ = 1, 5, 10, 25, 50, 75, 100 μM).

310–350 nm with an excitation wavelength of 290 nm. The measurements were carried out at temperatures of 298.1, 302.1, 306.2, 310.0, 314.3 K. The temperature control accuracy was $\Delta T = \pm 0.3$ K. The RatCol concentration was 10 μM, the atranorin concentration varied in the range of 1–30 μM with a step of 5 μM.

The effect of atranorin on the esterase activity of HSA was carried out at a wavelength of 405 nm using an Allsheng microplate photometer (China). For this purpose, the following solutions were prepared: 4-nitrophenylacetate (NPA) in isopropanol, HSA and atranorin in PBS (pH 7.02). Details of the experimental technique are described in the

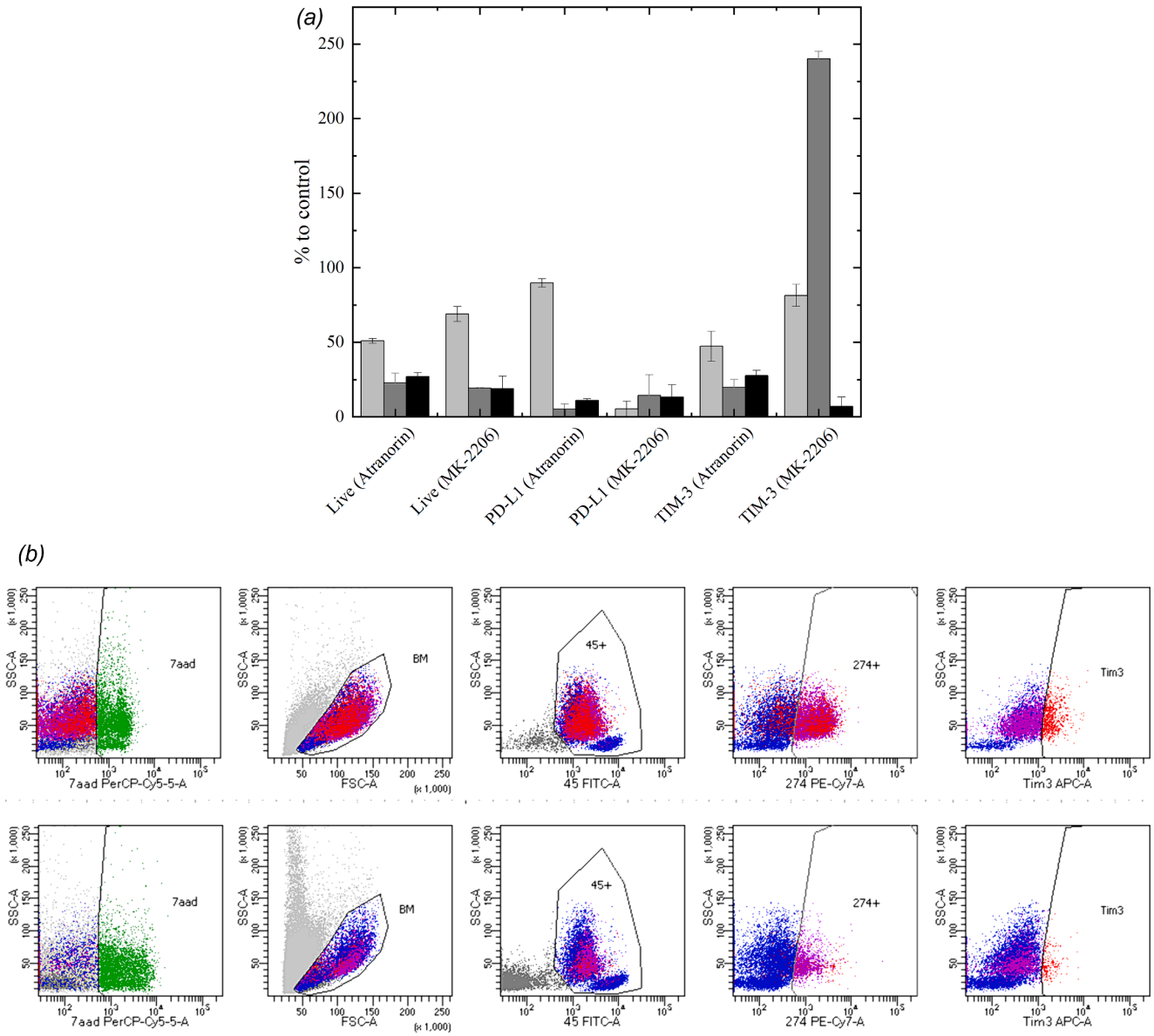


**Fig. 15.** Flow cytometry results: number of living cells relative to control, level of decrease in TIM-3 expression relative to control, PD-L1 relative to control (light grey — KG-1, dark grey — THP-1, dark — Mono-Mac-1) (*a*), example of decreased expression of TIM-3 and PD-L1 in the bone marrow when treated with atranorin (*b*). BM – Bone marrow cells, SSC-A – Side scatter area, FSC-A – Forward scatter area, 7aad – 7-Aminoactinomycin D, PerCP-Cy5-5-A – Peridinin chlorophyll protein-Cyanine5.5 area, FITC-A – Fluorescein-5-isothiocyanate, PE-Cy7-A – Phycoerythrin Cyanine7 area, Tim3 APC-A – Allophycocyanin-conjugated TIM-3 monoclonal antibody, 45 – CD45+-cells, 274 – CD274+-cells.

work [25].

The stable radical DPPH was used to study antiradical activity [26,27]. The measurements were carried out on a Thermo Scientific Evolution 300 spectrophotometer (USA). The detailed experimental procedure is described in the work [25]. Also, to study the antiradical activity, a model reaction with the stable radical anion ABTS (2,2′-azino-*bis*-(3-ethylbenzthiozoline-6-sulfonic acid) diammonium salt) was used. The experiment was carried out according to the method described in the work [28].

Experiments to study photoinduced haemolysis in the presence of atranorin were carried out according to the method described in refs. [29–32].

The study of the thermodynamic characteristics of the binding of atranorin to DNA and HSA was carried out by the Isothermal titration calorimetry (ITC) method using a TA Instruments Nano ITC 2G microcalorimeter (USA) equipped with a 1 ml gold measuring cell according to the method described in the work [33]. Based on the experimental data obtained, the interaction parameters of atranorin with DNA and HSA were calculated using the thermodynamic model of independent binding (Independent model) [34].

Experiments on thermal denaturation of DNA in the presence of atranorin were carried out on a Thermo Scientific Evolution 300 spectrophotometer (USA) with a thermostated cell in a 0.015 M NaCl solution in the temperature range 25–95 °C.

The cytotoxicity of atranorin was studied using the MTT method on the cell lines Human Umbilical Vein Endothelial Cells (ECV340) and Human Embryonic Kidney 293 (HEK293) [24,29,31,35].

To study the genotoxicity, the pBR322 plasmid (Thermo Fisher Scientific, USA) was propagated in the bacterial strain *Escherichia coli* DH5 alpha and isolated using the Plasmid MidiPrep kit (Evrogen, Russia) [36]. Concentrations of atranorin varied in the range of 10–100 μM; samples were incubated for 15 h at 37 °C and analysed by electrophoresis in 1 % agarose gel.

Also, the genotoxicity of atranorin was assessed using the DNA comet

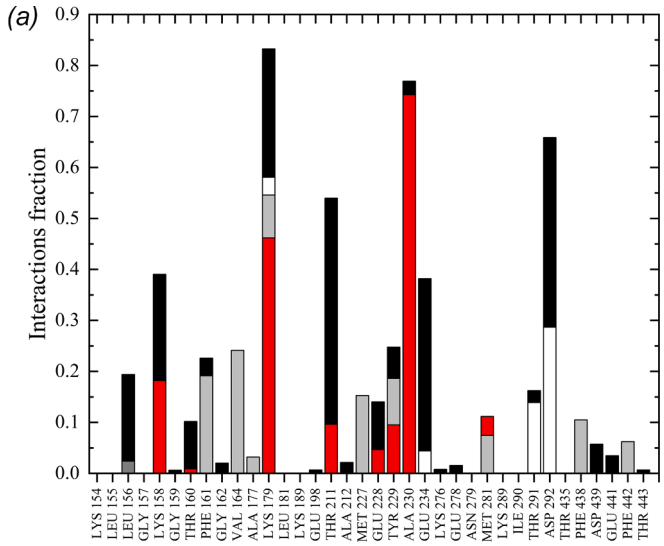


**Fig. 16.** AKT1 protein interactions with ATR within the ATP-competing site are monitored throughout the simulation of MD for 300 ns. Simulation interactions diagram panel of protein–ligand interactions (or 'contacts') categorised into four types: hydrogen bonds (red), hydrophobic (grey), ionic (white) and water bridges (dark) (*a*). The stacked bar charts are normalised over the course of the trajectory showing the fraction of the simulation time that each specific interaction was maintained throughout the MD run. A schematic representation of detailed ligand atom interactions with the protein residues (dashed circle — hydrophobic, dark grey circle — charged (negative), circle — charged (positive), light blue — polar, green — metal coordination, dark wavy line – Pi-Pi stacking, light grey circle — solvent exposure) (*b*). Interactions that occur more than 10.0 % of the simulation time in the selected trajectory (0.00 through 300.09 ns), are shown. The fraction of the simulation time normalized over the course of the trajectory that each specific interaction (shown by arrow) was maintained throughout the MD run. The threshold of 10% is represented.

assay, based on measuring the effect of substances under study on the DNA integrity of human PBMCs using alkaline microgel electrophoresis [35]. DNA comets were visualised using a Micromed 3 LUM fluorescence microscope (Russia). The tail lengths were measured using the CASP software (version 1.2.2). Tail DNA content and tail length were determined experimentally; tail momentum was calculated as the percentage of tail DNA multiplied by the distance between the centre of the head and tail [37].

### 2.3. Cell cultures and flow cytometry

Cells from the human monocytic leukaemia THP-1, acute myelogenous leukaemia KG-1 and human monocytic cell line Mono-Mac-01 were selected for testing. The cell experiments were carried out using known allosteric AKT inhibitor 8-[4-(1-aminocyclobutyl)phenyl]-9-phenyl [1,2,4]triazolo[3,4-f]-[1,6]naphthyridin-3(2H)-one (MK-2206, Sigma-Aldrich, USA) and atranorin. The cells were cultivated in RPMI-1640 (Biolot, Russia) medium, containing 10 % FBS (bioFroxx, Germany). The cell lines used in the work were provided by the Russian Collection of Cell Cultures of the Institute of Cytology, Russian Academy of Sciences. In the experiment, in each well of a plate for suspension cultures (Nest, China) $2{\cdot}10^5$ cells were added with the required volume of atranorin in a 2 ml culture medium. As controls, cells were used in the same amount and medium without the addition of atranorin, as well as with the addition of DMSO in the same concentration. Cells were cultured for 24 h at 37 °C under 5 % $CO_2$ until further cytofluorimetric analysis.

Nucleated bone marrow cells were isolated from the bone marrow aspirate of Acute Myeloid Leukaemia (AML) patients according to the standard protocol of erythrocyte lysis. Cells were used in the experiments immediately. Bone marrow was cultured in a culture medium RPMI-1640 (Biolot, Russia), containing 10 % FBS for 24 h at 37 °C under 5 % $CO_2$ until further cytofluorimetric analysis.

Flow cytometry was carried out on a FACSCanto II (BD Bioscience, USA). The cytometer was calibrated and the fluorescence baseline adjusted using the commercial BD FACS Diva SC&T Research Beads kit according to the manufacturer's recommendations. Monoclonal antibodies to TIM-3 (APC, Biolegend, clone A18087E), CD274 (PE-Cy7, Biolegend clone 29E.2A3) (Becton Dickinson, USA; Miltenyi Biotec, USA) were also used. Before assay ~$2{\cdot}10^5$ cells were transferred to a cytometric tube and centrifuged at 300 g for 7 min, after that washing off was done to a culture medium residues in 2 ml of CellWash (Becton Dickinson, USA), followed by centrifugation under the same conditions. Samples with antibodies were incubated for 15–20 min in the dark at room temperature. At the end of incubation, the cells were washed twice under the previous conditions. Samples were analysed by forward and side light scattering, stained with vital dye 7-AAD (PerCP-Cy5,5, Elabscience, China) or DRAQ7 (APC-Cy7, BioLegend, USA). Immediately before analysis, the sample volume was adjusted to 400 μl using CellWASH (Becton Dickinson, USA). Analysis of the obtained data was carried out using software BD FACSDiva Software.

In the experiments, due to the absence of a normal distribution, the obtained data are presented as a median and interquartile range (25th and 75th percentile), minimum and maximum values. The significance of differences between multiple groups was determined using Kruskal–Wallis test, *p*-value of less than 0.05 was considered statistically significant.

Statistical analysis was performed using SciPy (Virtanen et al., 2020), Pandas (Wes McKinney, 2010) Python (v.3.7) packages. Plotting was performed using R 4.3.1.

### 2.4. Computer modelling of the interaction of atranorin with AKT kinase

#### 2.4.1. Protein targets selection

AKT protein was chosen to study molecular interactions with atranorin. There are two binding sites known where the AKT-inhibition mechanism can be realised *via* conformational changes of the protein: ATP-competing site and allosteric inhibition [38]. Therefore, it was decided to study both binding sites of AKT. The protein model of AKT1 with selective ATP-competitive inhibitor AZD5363 (PDB ID 4GV1) was chosen; the model PDB ID 3O96 represented the crystal structure of AKT1 bound with selective allosteric inhibitor. The sequences of AKT1,2,3 were also retrieved from the UniProt Knowledge database. All

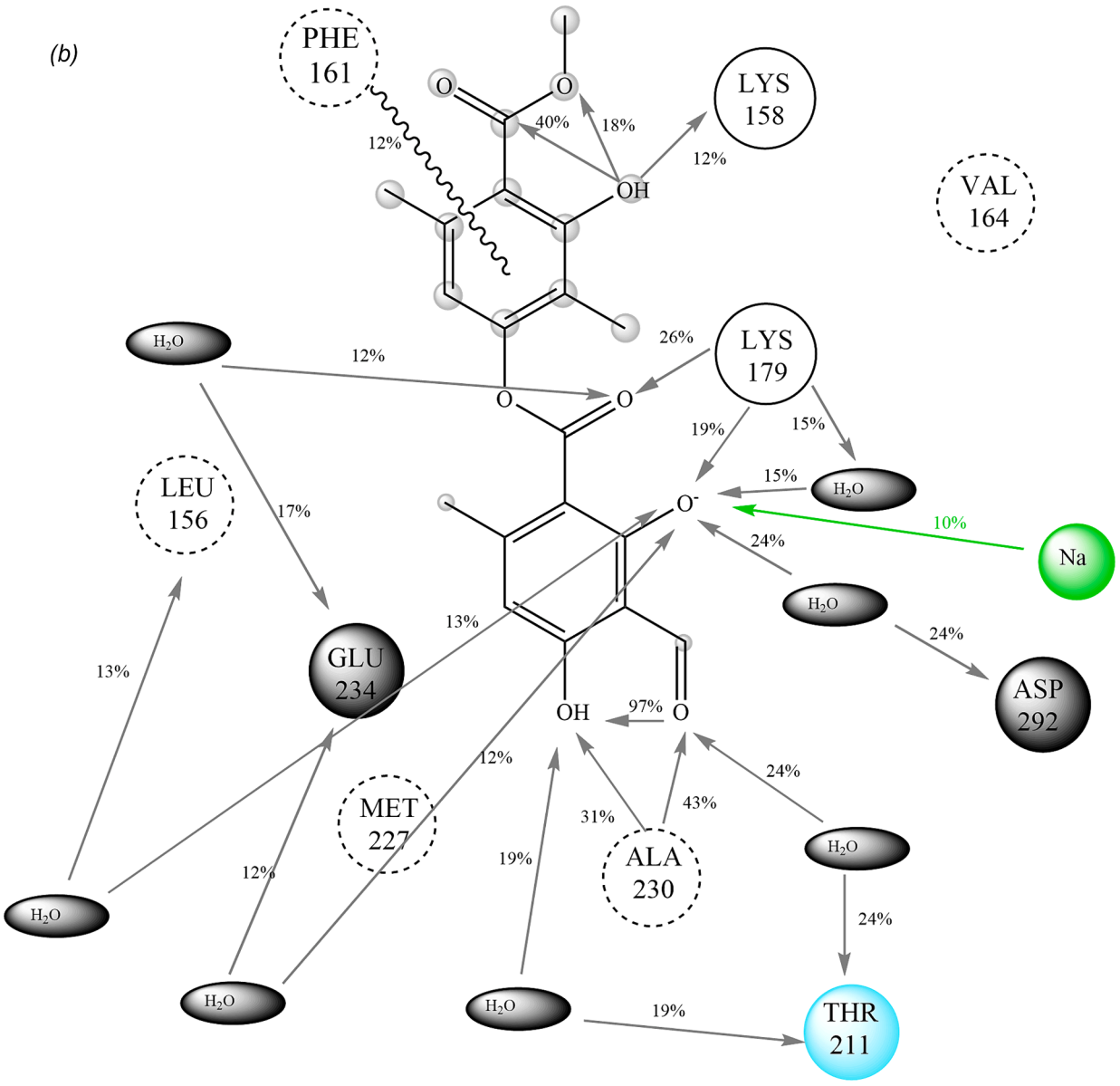


**Fig. 16.** (*continued*).

stages of protein modelling, docking, molecular dynamics (MD) and analytical calculations were performed using the Schrödinger molecular modelling suite (version 2021–1) (Schrödinger, LLC, New York, NY, 2021). The initial protein models 4GV1 and 3O96 were structurally aligned in order to evaluate the colocalisation of two inhibition sites: the alignment score was 0.211; resulting RMSD was 2.287 Å. The protein binding sites were evaluated within 5 Å of bound ligands; the amino acids composition was compared using The Schrödinger Maestro multiple sequence viewer (MSV).

### 2.4.2. *AKT1,2,3 homology modelling and preparation*

The quality of 4GV1 and 3O96 protein structures were tested and preprocessed in the Protein Preparation Wizard (PPW) [39]. Detected problems with invalid atom types (missing hydrogens, wrong number of bonds), alternate positions, steric clashes and other deviations were refined in PPW. The bond orders were assigned, and hydrogens were added after removal of the original hydrogens. Missing loops and side chains were checked in using Prime [40,41], possible protonation states were generated using EPIK state penalty under default parameters (pH 7.0±2.0) [42]. No problems were reported in the preprocessed protein structures. Additionally, the quality of complexes was analysed in the Protein Reliability Report; the initial protein–ligand complexes were refined in Prime (only some steric clashes were remained as no additional MD relaxation was made in order not to change the binding site conformation with ligand bound before docking studies for proper grid generation, especially for allosteric site model).

In order to test the allosteric site inhibition of other AKT homologs, the structures of AKT2 and AKT3 proteins were obtained by homology modelling on the AKT1 template PDB ID 3O96 using Schrodinger Homology Modeling Module [40,41], secondary structure prediction was carried out using the ClustalW alignment method, which works best for structures with high sequential similarity [43]. Models were aligned and further built using an energy-based method where the ligand was included into the final models.

### 2.4.3. *Ligand preparation*

The structure of ligand, atranorin, was retrieved from the PubChem compound database (CID-68066) [44] and further subjected to ligand preparation (LigPrep) prior to docking. LigPrep is a robust collection of tools designed to prepare high quality, all-atom 3D-structures for small

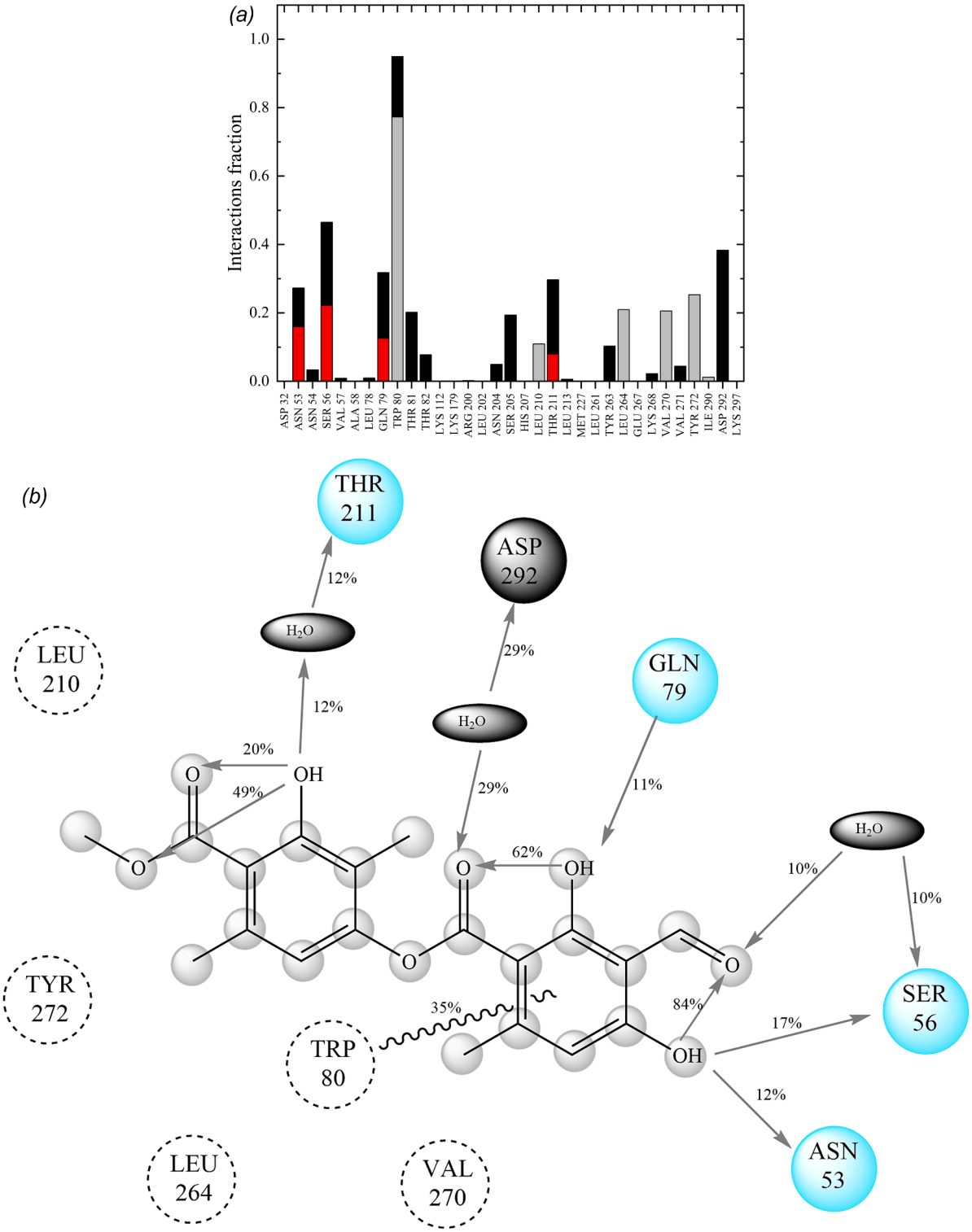


**Fig. 17.** AKT1 protein interactions with ATR within the allosteric site are monitored throughout the simulation of MD for 300 ns. A) Simulation interactions diagram panel of protein–ligand interactions (or 'contacts') categorised into four types: hydrogen bonds (red), hydrophobic (grey), ionic (white) and water bridges (dark) (*a*). The stacked bar charts are normalised over the course of the trajectory showing the fraction of the simulation time that each specific interaction was maintained throughout the MD run. A schematic representation of detailed ligand atom interactions with the protein residues (dashed circle — hydrophobic, dark grey circle — charged (negative), light blue — polar, dark wavy line – Pi-Pi stacking, light grey circle — solvent exposure) (*b*). Interactions that occur more than 10.0 % of the simulation time in the selected trajectory (0.00 through 299.99 ns), are shown. The fraction of the simulation time normalized over the course of the trajectory that each specific interaction (shown by arrow) was maintained throughout the MD run. The threshold of 10% is represented.

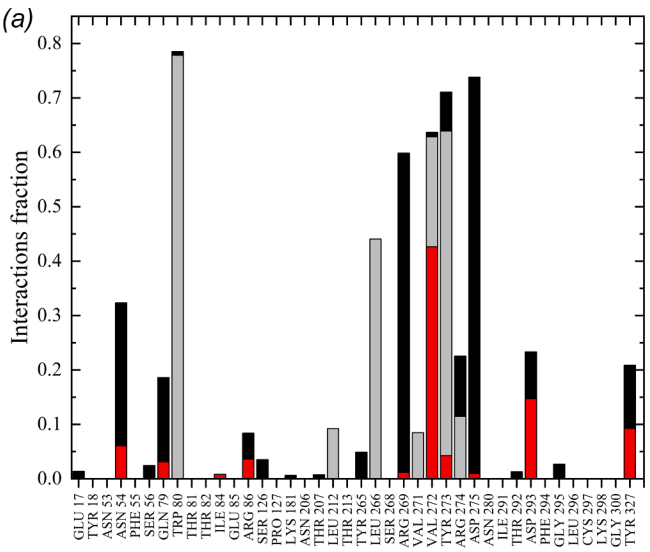


**Fig. 18.** AKT2 protein interactions with ATR within the allosteric site are monitored throughout the simulation of MD for 300 ns. Simulation interactions diagram panel of protein–ligand interactions (or 'contacts') categorised into four types: hydrogen bonds (red), hydrophobic (grey), and water bridges (dark) (*a*). The stacked bar charts are normalised over the course of the trajectory showing the fraction of the simulation time that each specific interaction was maintained throughout the MD run. A schematic representation of detailed ligand atom interactions with the protein residues (dashed circle — hydrophobic, dark grey circle — charged (negative), light blue — polar, dark wavy line – Pi-Pi stacking, red wavy line — Pi-cation, light grey circle — solvent exposure) (*b*). Interactions that occur more than 10.0 % of the simulation time in the selected trajectory (0.00 through 300.09 ns), are shown. The fraction of the simulation time normalized over the course of the trajectory that each specific interaction (shown by arrow) was maintained throughout the MD run. The threshold of 10% is represented.

molecules. This tool is also capable of generating multiple structures from input structure with various ionisation states, tautomers, stereochemistry, and ring conformations, as well as eliminating molecules using specified criteria. Atranorin for this study was also prepared by optimising geometries through OPLS4 [45] force field and ionisation of possible state were generated at pH 7.0±2.0 by EPIK [42]. Desalt and generate tautomers were also selected and the stereoisomer computation was checked to retain specific chirality (vary other chiral centres) and to generate at most 32 conformations per ligand. Finally, six atranorin tautomers were generated by LigPrep.

### 2.4.4. Receptor grid generation

Receptor grid was located at the bound ligand of AKT protein within the appropriate binding site. Grid box was defined around the co-crystallised ligand binding site and using Glide's Receptor-Grid-Generation tool. The grid was a cubic box, centred at the centroid of the ligand within the complex. In Glide [46], the grid was generated keeping the default parameters of van der Waals forces (vdW) scaling factor 1.0 and charge cut-off 0.25 using initial partial charges, subjected to OPLS4 force field [45].

### 2.4.5. Glide extra precision (XP) ligand docking

The atranorin docking was carried out inside the assigned grid box using the Ligand Docking tool within the Glide panel in the Schrödinger suite. The non-polar atoms were set for the VdW radii scaling factor by 0.8, the partial charge cut-off was 0.15 as well as using input partial charges. All docking settings were set to default except for the docking protocol that was changed to an extra precession (XP) mode [47] with flexible ligand sampling combined with sampling of nitrogen inventions and ring conformations; EPIK state penalties were added to docking score calculation; counting of aromatic H as donors was included into H-bonds. The post-docking minimisation was performed for resulting complexes. The generated atranorin-AKT complex with highest XP-GScore was applied for further MD simulation and analysis.

### 2.4.6. Molecular dynamics simulations

MD simulations were performed using the Desmond package [48]. The MD system was set-up in the Maestro's 'System Builder' utility as follows: TIP3P water model [49] was used to simulate water molecules; buffer distance in orthorhombic box was set up at 10 Å; recalculated amount of $Na^+/Cl^-$ ions were added to balance the system charge and were placed randomly to neutralise the solvated system; additional salt was appended for final concentration 0.15 M in order to simulate physiological conditions.

MD simulations were conducted with the periodic boundary conditions in the NPT ensemble class using OPLS4 force field parameters [45]. The temperature and pressure were kept at 300 K and 1 atmospheric pressure, respectively, using Nosé–Hoover temperature coupling and isotropic scaling [50]. The model system was relaxed before simulations using Maestro's default relaxation protocol including two stages of minimisation (restrained and unrestrained) followed by four stages of MD runs with gradually diminishing restraints. MD simulations were carried out by running the 300 ns recording the trajectory configurations obtained at 50 ps intervals. RMSD clustering was performed in the Desmond package [48]; total system energy was calculated by Prime [40,41].

### 2.4.7. Analysis of MD simulation

The MD trajectory files were investigated by using simulation quality analysis (SQA) and simulation interaction diagram (SID) programs available within the Desmond module: SID was employed to generate the protein and ligand's root mean square fluctuations (RMSF) and root mean square deviation (RMSD), ligand interaction fingerprints and interaction fractions with the proteins. The Prime module in Schrödinger suite 2021-1 was used to compute the ligand binding energies through the use of a physics-based MM/GBSA method [51,52]. MM/GBSA free energy of binding ($\Delta G_{bind}$) is calculated for the representative complex with minimal total energy from clustered Desmond trajectories using the equation: $\Delta G_{bind} = E_{Complex} - E_{Ligand} - E_{Receptor}$, where $E_{Complex}$, $E_{Ligand}$, and $E_{Receptor}$ are the energy calculations done in Prime MM/GBSA of the optimised complex (complex), optimised free ligand (ligand), and optimised free receptor (receptor). The OPLS4 force field and VSGB solvation model were used in the calculations.

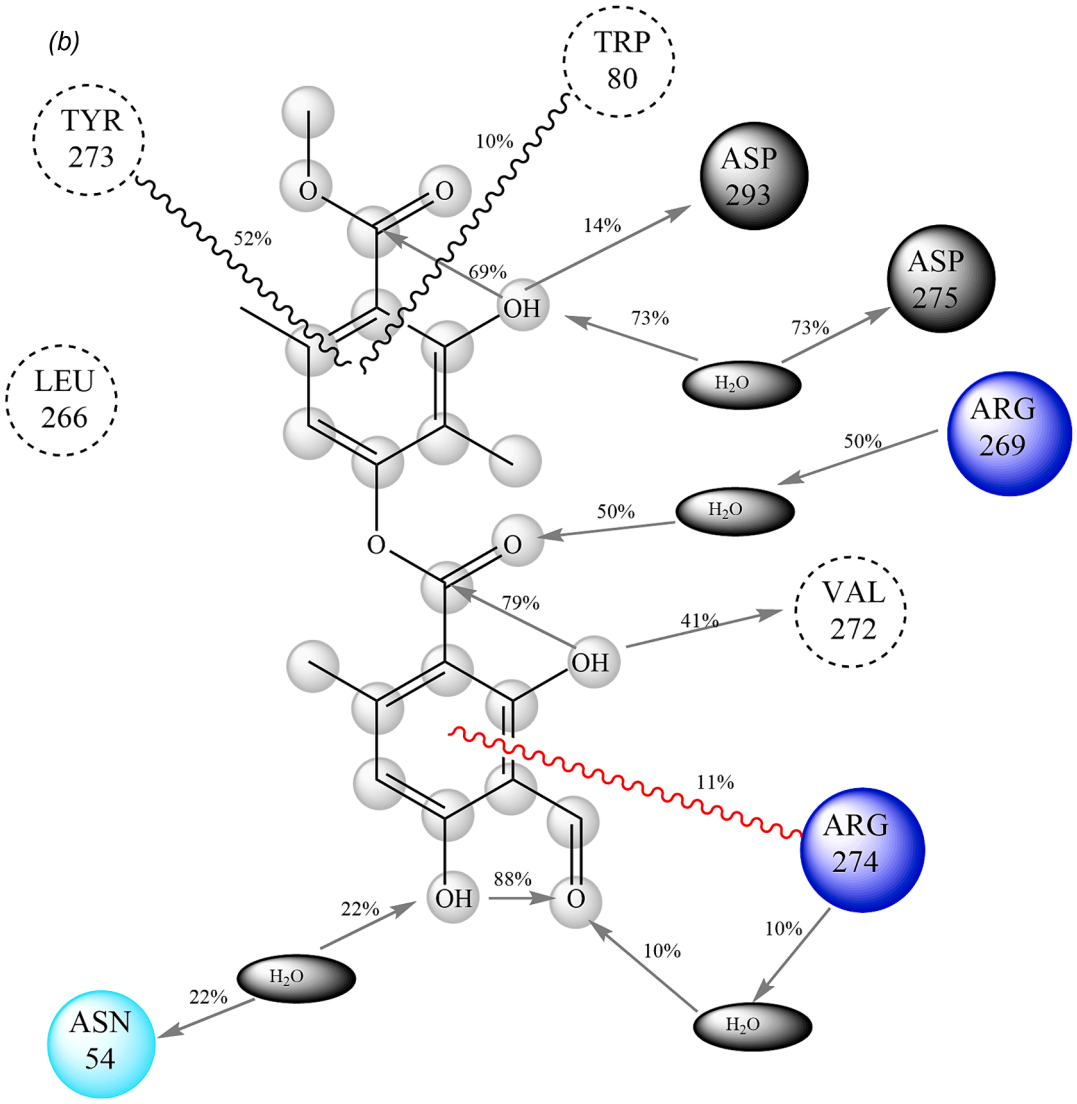


**Fig. 18.** (*continued*).

## 3. Results and discussion

### 3.1. Partition coefficient

The distribution coefficient of atranorin in the octan-1-ol–water system was calculated using the formula:

$$P_{ow} = \frac{c'_o}{c'_w} = \frac{c_w - c'_o}{c'_w} \quad (1)$$

where $c_o$' and $c_w$' are concentrations of atranorin in octan-1-ol and water, respectively, after achieving equilibrium, $c_w$ is the initial concentration of atranorin in water.

The resulting lg$P_{ow}$ value for atranorin was 1.22. The obtained value indicates that atranorin has lipophilic properties. A lg$P_{ow}$ value between −1 and +2 is considered optimal for substances intended for oral administration [53]. With a low lg$P_{ow}$ value, the compound will be poorly absorbed and, as a result, have low bioavailability.

### 3.2. Haemocompatibility

To study the haemocompatibility of atranorin, its effect on spontaneous haemolysis was determined. Fig. 6 shows the concentration dependence of the degree of haemolysis in the presence of atranorin after 1 and 3 h. Analysis of the results obtained indicates that atranorin can be considered haemocompatible in the concentration range of 1–100 μM since the degree of haemolysis does not exceed 5 % [30,54,55].

Table 2 provides data on the study of the effect of atranorin on ADP-, collagen-, and adrenaline-induced platelet aggregation. As a result a weak pro-aggregant activity of atranorin was revealed in the concentration range of 1–100 μM for ADP- and collagen-induced platelet aggregation. At the same time addition of adrenaline caused moderate pro-aggregant activity of atranorin.

To identify the putative mechanism of the effect of atranorin on platelet aggregation, the binding constants ($K_b$) and stoichiometry ($n$) of the binding process with RatCol were determined using the Scatchard equation:

$$\lg\frac{F_0 - F}{F} = \lg K_b + n\lg Q \quad (2)$$

where $F_0$ is the fluorescence intensity of RatCol in the absence of atranorin, $F$ is the fluorescence intensity of RatCol in the presence of atranorin, $Q$ is the molar concentration of atranorin, μM. From the dependence in Hill coordinates $\lg\frac{F_0-F}{F}$ *vs* lg$Q$ (Fig. S2), $K_b$ values were identified for binding of atranorin to RatCol (Table 3) [56–58]. The obtained binding constants indicate that atranorin forms a stable

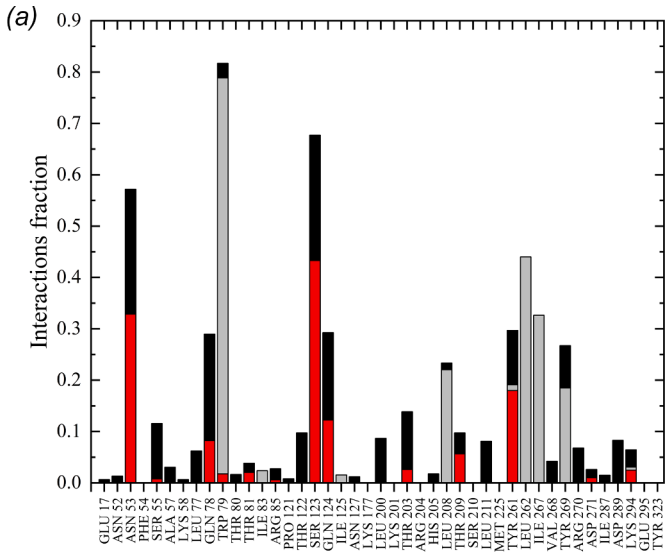


**Fig. 19.** AKT3 protein interactions with ATR within the allosteric site are monitored throughout the simulation of MD for 300 ns. Simulation interactions diagram panel of protein–ligand interactions (or 'contacts') categorised into four types: hydrogen bonds (red), hydrophobic (grey), and water bridges (dark) (*a*). The stacked bar charts are normalised over the course of the trajectory showing the fraction of the simulation time that each specific interaction was maintained throughout the MD run. A schematic representation of detailed ligand atom interactions with the protein residues (dashed circle — hydrophobic, light blue — polar, dark wavy line – Pi-Pi stacking, light grey circle — solvent exposure) (*b*). Interactions that occur more than 10.0 % of the simulation time in the selected trajectory (0.00 through 300.04 ns), are shown. The fraction of the simulation time normalized over the course of the trajectory that each specific interaction (shown by arrow) was maintained throughout the MD run. The threshold of 10% is represented.

complex with RatCol.

Determination of changes in enthalpy and entropy of the binding reaction of atranorin with RatCol were calculated using the van't Hoff equation:

$$\ln K_b = -\frac{\Delta H}{RT} + \frac{\Delta S}{R} \quad (3)$$

where $\Delta H$ and $\Delta S$ are changes in the enthalpy and entropy of the binding reactions of atranorin with collagen, $R$ is the gas constant, $T$ is the absolute temperature.

The change in the Gibbs energy ($\Delta G$) of the binding reaction of atranorin with RatCol in the temperature range 298.2–314.3 K was calculated using the formula:

$$\Delta G = \Delta H - T\Delta S \quad (4)$$

Negative $\Delta G$ values (Table 4) in the temperature range 298.2–314.3 K indicate that the binding of atranorin to RatCol is thermodynamically favourable. The positive $\Delta H$ and $\Delta S$ values indicate that atranorin binds to RatCol primarily through hydrophobic interactions.

Regarding data on the interaction of atranorin with RatCol with data on platelet aggregation, it can be seen that atranorin forms a fairly strong complex with collagen. However, most likely, the active center of collagen, which is responsible for interaction with the platelet GPVI receptor, is not involved [59]. This fact leads to an increase in collagen-induced platelet aggregation.

The dependence of the thermal effect of the reaction of interaction of atranorin with HSA at 298.15 K on the titrant concentration (HSA) is presented in Fig. 7. It can be seen that in this case there is an endothermic thermal effect. Based on the experimental data obtained, the interaction parameters of atranorin with HSA were calculated using the thermodynamic model of independent binding (independent model) [34] (Table 5). It can be seen that atranorin forms a moderately strong complex with HSA. Thus, HSA will perform a transport function in the bloodstream [60].

The first order reaction equation was used to determine the rate constant for NPA hydrolysis [25].

$$\ln\left(1 - \frac{A_t - A_0}{A_{NF}}\right) = -kt \quad (5)$$

where $A_{NF}$=1.86 is the optical density of *p*-nitrophenol solution ($C$=100 μM); $A_t$ is the optical density of the reaction mixture at time $t$; $A_0$ is the optical density of the reaction mixture at the initial time; $k$ is the first order reaction rate constant ($min^{-1}$); $t$ is the time from the start of the reaction (min).

First-order rate constants of the reaction of the hydrolysis of NPA by HSA in the absence and presence of 50 μM atranorin were calculated from the slope of the straight lines in coordinates $\ln\left(1 - \frac{A_t - A_0}{A_{NF}}\right)$ *vs t*. Fig. 8 shows the dependence of the rate constants of the NPA hydrolysis reaction on the concentration of atranorin. It can be seen that the rate constants do not change in the presence of atranorin in the studied concentration range.

### 3.3. Study of the effect of atranorin on antioxidant properties

The degree of inhibition of free radical reactions involving DPPH and ABTS radicals was assessed using the equation:

$$I = \frac{A_{rad} - (A_{sample} - A_{blank})}{A_{rad}} \cdot 100\% \quad (6)$$

where $I$ is a fraction of reduced radicals (%); $A_{rad}$, $A_{sample}$, $A_{blank}$ are optical densities of solutions of radicals (DPPH or ABTS), solutions containing atranorin and stable radicals, and solutions of atranorin without radicals, respectively.

Fig. 9 shows the dependence of the proportion of reduced radicals on the concentration of atranorin. It can be seen that in the case of the reaction with DPPH, the $IC_{50}$ is 117 μM, in turn, the $IC_{50}$ value of ascorbic acid in this model reaction is less than 10 μM. In the model reaction of atranorin with ABTS, the $IC_{50}$ is less than 10 μM; for comparison, the $IC_{50}$ of ascorbic acid is 3.6 μM. From the data obtained, it follows that atranorin exhibits pronounced antiradical activity under experimental conditions, and in the case of a model reaction with ABTS

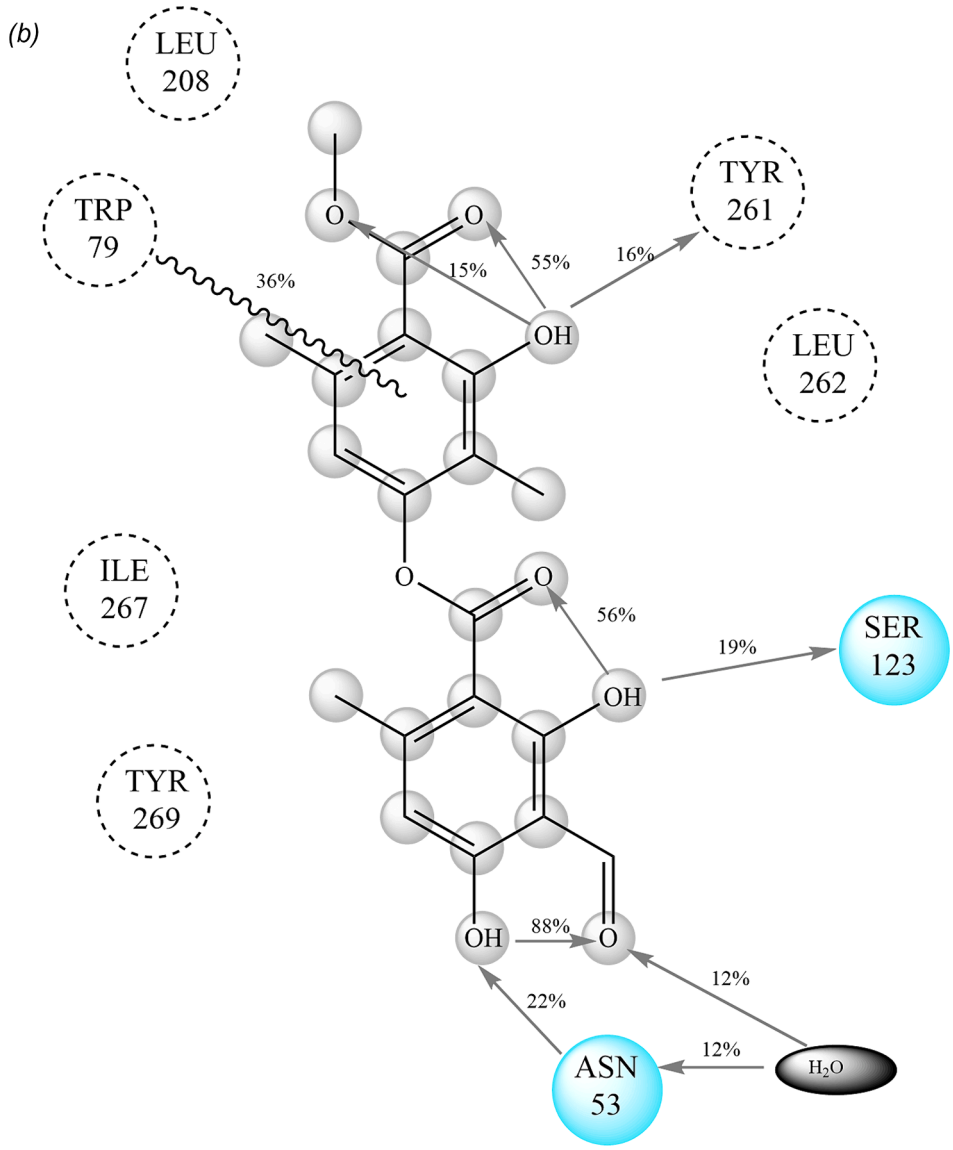


**Fig. 19.** (*continued*).

**Table 7**
MM/GBSA free energy of binding (Δ*G*-bind) of atranorin with AKT within the binding site calculated on the representative MD structure with minimal total energy.

| AKT protein | Δ*G*-bind/kcal·mol$^{-1}$ |
|---|---|
| AKT1 (ATP-competing site) | −20.89 |
| AKT1 (allosteric-inhibition site) | −52.09 |
| AKT2 (allosteric-inhibition site) | −63.65 |
| AKT3 (allosteric-inhibition site) | −68.77 |

it is comparable to ascorbic acid.

From the presented Fig. S3, it can be seen that atranorin in the studied concentration range (1–100 μM) has no effect on the level of photoinduced haemolysis.

### 3.4. Binding to DNA

Fig. 10 shows the dependence of the thermal effect of the reaction of interaction of atranorin with DNA at 298.15 K depending on the concentration of the titrant (atranorin). The resulting interaction stoichiometry shows that at the equivalence point there are 1.2 mol of DNA per 1 mol of atranorin (Table 5). The binding constant of atranorin to DNA obtained by ITC method ($K_b = 2.88{\cdot}10^4$) indicates moderate binding of DNA to atranorin.

The temperature at which 50 % of the double-stranded DNA remains in the double-stranded state is considered the DNA melting temperature ($T_m$) [61]. The melting temperature of DNA ($T_m$) directly depends on the stability of its double helix. The interaction of DNA with small molecules can stabilise the nucleic acid structure by causing conformational changes, which usually leads to an increase in the $T_m$ value. The melting curves of DNA and the DNA complex with atranorin are shown in Fig. 11. It can be seen that the melting temperature of the complex of atranorin with DNA ($T_m = 83.5$ °C) exceeds the melting temperature of DNA in a 0.15 M NaCl solution ($T_m = 78.9$ °C). It can be concluded that the interaction of DNA with atranorin stabilises the structure of the nucleic acid, causing conformational changes that lead to an increase in the $T_m$ value.

### 3.5. Cytotoxicity

Fig. 12 shows the effect of atranorin on the viability of the ECV340 and HEK293 cell lines, which implies that atranorin does not exhibit a

cytotoxic effect. It should be noted that atranorin exhibits a cytotoxic effect against tumour cell lines of acute monocytic leukaemia (THP-1), acute myeloid leukaemia (KG-1), and acute monocytic leukaemia Mono-Mac-1. Data from studies of the cytotoxicity of atranorin are consistent with data obtained by flow cytometry (see section 3.7).

### 3.6. Genotoxicity

Depending on the conformation, plasmid DNA molecules move differently during agarose gel electrophoresis. The molecules that are in the supercoiled state go farthest. Molecules containing a single-strand gap, which are in a relaxed state, pass the least. In the middle, linear molecules move between them, resulting from a double-strand break. The results of electrophoresis of 'native' plasmid DNA isolated from bacteria, as well as treated with enzymes that introduce single-strand or double-strand breaks into the molecules are presented in Fig. 13 (full gel in Fig. S6). At the concentrations used, atranorin do not cause a significant number of breaks in DNA, which could be determined using this method.

The mean values of % tail DNA, tail length, and comet tail momentum observed from human PBMCs incubated in the presence of $H_2O_2$ (positive control), PBS (negative control) and atranorin ($C$=1–100 μM) are presented in Table 6. It can be seen that the amount of DNA damage in the presence of $H_2O_2$ is significantly higher than in control cells. Thus, atranorin in the studied concentration range did not cause DNA damage and, therefore, did not have a genotoxic effect. As an example, Fig. 14 presents photographs of DNA comets in the presence of $H_2O_2$ ($C$=100 μM), PBS and atranorin (1, 5, 10, 25, 50, 75, 100 μM).

Previously, the genotoxic effect of atranorin has not been studied, but there is some information in the literature on the assessment of the genotoxic effect of another widespread lichen metabolite — usnic acid (UA). Using the DNA comet assay, it was found that treatment of V79 cells (cells exhibiting morphology of fibroblasts isolated from the lung of a male Chinese hamster) with UA caused a significant increase in the degree of DNA damage at concentrations of 60 – 120 $\mu g \cdot ml^{-1}$ compared to the control [62]. The same method was used to study the genotoxicity of the (+) and (–) enantiomers of UA in human lymphocytes, revealing that the enantiomers exhibited a genotoxic effect at concentrations of 12.5 – 100 $\mu g \cdot ml^{-1}$, while the genotoxicity of (–) UA at concentrations exceeding 50 $\mu g \cdot ml^{-1}$ was 2.0 times higher than that of the (+) UA [63]. The genotoxic effect of UA in doses of 50 and 100 mg / kg in the liver and kidney cells of mice was observed 1 h after oral administration The genotoxic effect of UA is mainly associated with oxidative stress in cells [64].

### 3.7. Flow cytometry

The effect of atranorin on the expression of TIM-3 and PD-L1 was studied on cell lines KG-1, THP-1, Mono-Mac-01. The following parameters of reduction in cell viability were revealed (Fig. 15*a*): for KG-1, viability decreased from (90.92±2.85) % to (64.60±16.15) %, for THP-1 from (88.6±5.30) % to (20.45±6.43) %, for Mono-Mac-1 from (81.73 ±2.40) % to (22.10±2.76) %. For KG-1, the PD-L1 level decreased from (77.97±5.45) % to (53.67±27.38) %, for THP-1 from (92.2±6.04) % to (4.95±5.16) %, for Mono-Mac-1 from (97.87±0.25) % to (26.87±4.87) %. For KG-1, the level of TIM-3 decreased from (77.2 ± 0.7) % to (75.67 ±1.06) %, for Mono-Mac-1 from (43.77±1.01) % to (4.77±0.85) %, on THP-1 TIM-3 is underrepresented. After a series of experiments, only Mono-Mac-01 showed statistical significance for TIM-3 and PD-L1 ($p$-value = 0.0495). The remaining crops did not show statistical significance. Similar results were obtained on human bone marrow cells under the influence of atranorin. The expression of TIM-3 and PD-L1 was reduced by 6.1- and 3.4-fold, respectively (Fig. 15*b*).

The known low molecular weight AKT inhibitor MK-2206 dihydrochloride (30 μM) was also tested and had a similar effect (Fig. 15*a*). In the KG-1 cell line addition of MK-2206 resulted in reduced expression of PD-L1 from (81.3±5.3) % to (4.3 ± 4.2) %, TIM-3 from (82.9±4.6) % to (21.9±7.6) % ($p$ = 0.006). In THP-1 cell line downregulation of PD-L1 was observed after exposure to 30 μM of MK-2206 from (87.4±20.04) % to (12.5±12.1) % ($p$ = 0.002). In Mono-Mac-1 cell line was a significant downregulation of PD-L1 after exposure with MK-2206 from (97.26±1.14) % to (12.9±8.0) % ($p$ = 0.006), TIM-3 expression in Mono-Mac-1 cell lines decreased from (53.25±15.25) % to (3.6±3.4) % ($p$ = 0.006).

### 3.8. Computer modelling of the interaction of atranorin with AKT kinase

AKT is the key protein in the PI3-kinase pathway involved in cellular metabolism, growth, proliferation, differentiation, and survival of cells. It was shown that AKT is overexpressed constitutively due to its own mutation of upstream proteins in the cancers [65,66]. Hence, inhibiting the AKT has been reported to adjuvant cancer therapy to increase patient survival. There have been extensive efforts to develop AKT inhibitors as therapeutics due to the involvement of oncogenic activating mutations in PI3K and AKT in cancer and overgrowth disorders [67–69]. Thus, the AKT protein was chosen as a potential target for atranorin binding. There are two binding sites known where the AKT-inhibition mechanism can be realised *via* conformational changes of the protein: ATP-competing site and allosteric inhibition [38]. Therefore, it was decided to study both binding sites for binding with atranorin. The protein model of AKT1 with selective ATP-competitive inhibitor AZD5363 (PDB ID 4GV1) was chosen; the model PDB ID 3O96 represented the crystal structure of AKT1 bound with selective allosteric inhibitor. Comparison details of both inhibition sites between AKT homologs (in supplementary information) revealed that all AKT proteins are similar at the binding ATP-competing site, therefore, one AKT homolog (e.g., AKT1) would be a representative structure for interaction studies of atranorin binding *via* ATP-competing site. However, analysis of allosteric-inhibition site sequences revealed significant differences in amino acid composition of AKT1, AKT2 and AKT3 proteins. Therefore, three homologous models of AKT1,2,3 should be generated for docking studies as the sequence differences might influence interaction interface and subsequent structural changes during allosteric inhibition of the protein.

Total 6 atranorin hits were prepared for further docking studies with AKT proteins. The preparation included converting the 2D-structure to energy-minimised 3D-structure and generating all possible ionisation and tautomeric states using Schrodinger's LigPrep tools. Moreover, ADME properties were predicted for all generated atranorin hits using QikProp [70] (Table S2). ADMET results and description is into supplementary information.

Docking of atranorin with AKT proteins were performed using extra precision XP-Glide. Top-complexes with the highest XP GScore obtained after docking into each inhibition site of AKT (ATP-competitive (AKT1-model) and allosteric (AKT1,2,3-models)) further were subjected to molecular dynamics (MD) run for 300 ns. MD simulates the dynamic behaviour of the molecular system under computer-generated physiological conditions to assess the protein–ligand complex stability over the time and binding affinity [71]. The protein–ligand complex stability is assessed by the RMSD plot, which measures the deviation of the protein and ligand atoms positions inside the binding pocket at the end of the simulation period (300 ns) compared to their initial positions before the simulation at 0 ns. RMSD analysis demonstrated more stability of atranorin molecule within the AKT2 and AKT3 complexes docked into allosteric sites (Fig. S4) where less sharp fluctuations of the ligand were observed during 300 ns MD run. However, RMSD plots of all AKT-atranorin complexes showed the atom fluctuations were within the acceptable range of 1–3 Å, and atranorin RMSD values do not significantly exceed the RMSD values of the protein, indicating quite stable behaviour of atranorin at both binding pockets throughout the simulation period (Fig. S4).

The major interactions and bond dynamics of atranorin within the

both binding sites were demonstrated *via* 300 ns MD simulation (Figs. 16–19, Fig. S5). The main binding pattern of AKT1 ATP-competing site consists Lys158, Lys179, Ala211, Thr230 forming H-bonds along with Glu234, Thr291 and Asp292 through water bridges and ionic bonds with the hydroxyl and carbonyl groups of atranorin. Additional hydrophobic interactions were formed by Phe161, Val164, Met227 and Phe438, Phe442 which additionally stabilised the benzene rings of atranorin. The key binding residues in the allosteric site of AKT were Gln79, Trp80 in all AKT proteins. Other interactions, their dynamics and impact varied depending on the AKT homolog, but the common interacting interface can be revealed within the allosteric site mainly *via* cumulative hydrophobic interactions, H-bonds and water-bridges (Figs. 16–19, Fig. S5). The main binding pattern of AKT1 within the allosteric sites was Asn53, Ser56, Glu79, Thr80, Thr211, Leu264, Val270, Tyr272, Asp292. The key binding residues of AKT2 in the allosteric site were Asn54, Gln79, Trp80, Leu266, Arg269, Val272, Tyr273, Asp275, Asp293, Tyr327. The essential binding pattern within the AKT3 binding site consisted of Asn53, Gln78, Trp79, Ser123, Gln124, Leu208, Tyr261, Leu262, Ile267, Tyr269. Additionally, the strength of ATR interaction was calculated within both binding sites of AKT homologs. The binding ΔG was calculated *via* MM-GBSA method on the representative structure with minimal total energy (Table 7). The resulting Δ*G*-bind corresponds to the initial XP-docking score, and it can be concluded that the preferred binding of ATR occurs in the allosteric site with the maximum binding strength within the complex of AKT3 protein.

## 4. Conclusion

In this work, a comprehensive study of the biocompatibility, cytotoxicity and genotoxicity of atranorin, a secondary aromatic metabolite of a number of lichens, was carried out. The compound was characterised using a complex of physicochemical methods of analysis: UV, IR, NMR spectroscopy, mass spectroscopy, elemental analysis. The biocompatibility study included the study of haemocompatibility, antiradical activity, cytotoxicity against the ECV340 and HEK293 cell lines, as well as genotoxicity using the pBR322 plasmid and the DNA comet method. It has been shown that atranorin does not cause haemolysis, exhibits weak pro-aggregant activity, forms a stable complex with HSA ($K_b = 7.6{\cdot}10^4$ $M^{-1}$) and DNA ($K_b = 2.88{\cdot}10^4$ $M^{-1}$), and has pronounced antiradical properties in model reactions with radicals DPPH and ABTS, and is also non-cytotoxic (to non-tumour cell lines ECV340 and HEK293) and does not exhibit genotoxicity. Atranorin has previously been shown to be an AKT kinase inhibitor. The present study found that the consequence of this is a decrease in AKT-dependent expression of PD-L1 and TIM-3. In addition, molecular modelling of atranorin-AKT complexes showed stable interaction of the atranorin molecule with proteins, with the greatest binding strength at the allosteric site of AKT3 inhibition.

## CRediT authorship contribution statement

**Konstantin N. Semenov:** Writing – review & editing, Project administration, Formal analysis, Data curation, Conceptualization. **Ilya A. Prokopiev:** Writing – original draft, Methodology, Investigation. **Natalya V. Petukhova:** Writing – review & editing, Software, Investigation, Conceptualization. **Uliana A. Kremenetskaya:** Investigation. **Dina A. Senichkina:** Writing – original draft, Investigation. **Olga S. Epifanovskaya:** Writing – original draft, Investigation. **Andrei M. Rumiantsev:** Investigation, Data curation. **Pavel A. Andoskin:** Writing – original draft, Investigation, Data curation. **Jasur A. Rizaev:** Writing – review & editing, Investigation, Formal analysis. **Dilafruz K. Kholmurodova:** Writing – review & editing, Investigation, Formal analysis. **Sergei V. Ageev:** Writing – original draft, Investigation, Data curation. **Yurii A. Anufrikov:** Investigation, Data curation. **Egor E. Zakharov:** Investigation, Data curation. **Ivan S. Moiseev:** Writing – review & editing, Resources, Project administration, Methodology, Conceptualization. **Vladimir V. Sharoyko:** Writing – review & editing, Supervision, Methodology, Investigation, Data curation, Conceptualization.

## Declaration of competing interest

The authors declare that they have no known competing financial interests or personal relationships that could have appeared to influence the work reported in this paper.

## Data availability

Data will be made available on request.

## Acknowledgments

The work was carried out with the financial support of the Ministry of Health of the Russian Federation No. 123030200028-7 'Development of small molecule checkpoint modulators for the treatment of myelodysplastic syndrome'. The equipment of the following Resource Centres of the Research Park of Saint Petersburg State University was used: the Centre for Diagnostics of Functional Materials for Medicine, Pharmacology and Nanoelectronics, Magnetic Resonance Research Centre, Centre for Chemical Analysis and Materials Research, Thermogravimetric and Calorimetric Research Centre. The authors acknowledge Saint-Petersburg State University for a research project AAAA-A19-119082790069-6.

## Appendix A. Supplementary material

Supplementary material to this article can be found online at https://doi.org/10.1016/j.molliq.2024.125743.

## References

[1] J.A. Elix, E. Stocker-Wörgötter, Biochemistry and secondary metabolites, in: *Lichen Biology* 104–133, Cambridge University Press, 2008, https://doi.org/10.1017/CBO9780511790478.008.
[2] Hawksworth, D. L. Supplement to "Chemical and Botanical Guide to Lichen Products". By Chicita F. Culberson. The American Bryological and Lichenological Society (Reprinted from Bryologist, 73: (177–377). 1970. *The Lichenologist* **5**, 179–179 (1971).
[3] M.J. Calcott, D.F. Ackerley, A. Knight, R.A. Keyzers, J.G. Owen, Secondary metabolism in the lichen symbiosis, Chem. Soc. Rev. 47 (2018) 1730–1760.
[4] S. Shibata, Yasuhiko Asahina (1880–1975) and His Studies on lichenology and chemistry of lichen metabolites on JSTOR, Bryologist 103 (2000) 710–719.
[5] E. Studzinska-Sroka, A. Galanty, W. Bylka, Atranorin - an interesting lichen secondary metabolite, Mini-Rev. Med. Chem. 17 (2017).
[6] M. Kosanić, B. Ranković, T. Stanojković, A. Rančić, N. Manojlović, Cladonia lichens and their major metabolites as possible natural antioxidant, antimicrobial and anticancer agents, LWT - Food Sci. Technol. 59 (2014) 518–525.
[7] B. Ranković, M. Mišić, S. Sukdolak, The antimicrobial activity of substances derived from the lichens Physcia aipolia, Umbilicaria polyphylla, Parmelia caperata and Hypogymnia physodes, World J. Microbiol. Biotechnol. 24 (2008) 1239–1242.
[8] T.H. Vu, et al., Depsides: lichen metabolites active against hepatitis c virus, PLoS One 10 (2015) e0120405.
[9] L. Desmarets, Lichen or associated micro-organism compounds are active against human coronaviruses, Viruses 15 (2023) 1859.
[10] T. Kristmundsdóttir, E. Jónsdóttir, H.M. Ögmundsdóttir, K. Ingólfsdóttir, Solubilization of poorly soluble lichen metabolites for biological testing on cell lines, Eur. J. Pharma. Sci. 24 (2005) 539–543.
[11] K.C. Kumar, S.K. Müller, Lichen Metabolites. 2. antiproliferative and cytotoxic activity of gyrophoric, usnic, and diffractaic acid on human keratinocyte growth, J. Nat. Prod. 62 (1999) 821–823.
[12] N.B. Perry, et al., Antimicrobial, antiviral and cytotoxic activity of new zealand lichens, The Lichenologist 31 (1999) 627–636.
[13] E.R. Correché, R.D. Enriz, M. Piovano, J. Garbarino, M.J. Gómez-Lechón, Cytotoxic and apoptotic effects on hepatocytes of secondary metabolites obtained from lichens, Alternat. Lab. Animals 32 (2004) 605–615.
[14] F.J. Toledo Marante, A. García Castellano, F. Estévez Rosas, J. Quintana Aguiar, J. Bermejo Barrera, Identification and quantitation of allelochemicals from the lichen Lethariella canariensis: Phytotoxicity and antioxidative activity, *J. Chem. Ecol.* 29 (2003) 2049–2071.

[15] B. Ranković, M. Kosanić, N. Manojlović, A. Rančić, T. Stanojković, Chemical composition of Hypogymnia physodes lichen and biological activities of some its major metabolites, Med. Chem. Res. 23 (2014) 408–416.
[16] R. Zhou, The lichen secondary metabolite atranorin suppresses lung cancer cell motility and tumorigenesis, *Sci. Rep.* 7 (1) (2017) 1–13.
[17] A. Galanty, et al., Usnic acid and atranorin exert selective cytostatic and anti-invasive effects on human prostate and melanoma cancer cells, Toxicology in Vitro 40 (2017) 161–169.
[18] M. Bačkorová, M. Bačkor, J. Mikeš, R. Jendželovský, P. Fedoročko, Variable responses of different human cancer cells to the lichen compounds parietin, atranorin, usnic acid and gyrophoric acid, Toxicol. Vitro 25 (2011) 37–44.
[19] A. Russo, S. Caggia, M. Piovano, J. Garbarino, V. Cardile, Effect of vicanicin and protolichesterinic acid on human prostate cancer cells: Role of Hsp70 protein, Chem. Biol. Interact 195 (2012) 1–10.
[20] L.K. Rotter, et al., Epidemiology and pathogenesis of myelodysplastic syndrome, Cancer J. (United States) 29 (2023) 111–121.
[21] L. Malcovati, et al., Diagnosis and treatment of primary myelodysplastic syndromes in adults: recommendations from the European LeukemiaNet, Blood 122 (2013) 2943–2964.
[22] P.L. Greenberg, et al., NCCN Guidelines® Insights: Myelodysplastic Syndromes, Version 3.2022: Featured Updates to the NCCN Guidelines, J. Natl. Comprehens. Cancer Network 20 (2022) 106–117.
[23] A. Harikrishnan, et al., Atranorin, an antimicrobial metabolite from lichen *Parmotrema rampoddense* exhibited in vitro anti-breast cancer activity through interaction with Akt activity, J. Biomol. Struct. Dyn. 39 (2021) 1248–1258.
[24] O.V. Mikolaichuk, et al., Biocompatibility and bioactivity study of a cytostatic drug belonging to the group of alkylating agents of the triazine derivative class, J. Mol. Liq. 343 (2021) 117630.
[25] A.O.E. Abdelhalim, et al., Graphene oxide enriched with oxygen-containing groups: on the way to an increase of antioxidant activity and biocompatibility, Colloids Surf. B Biointerf. (2021) 112232, https://doi.org/10.1016/j.colsurfb.2021.112232.
[26] U.R. Farooqui, A.L. Ahmad, N.A. Hamid, Graphene oxide: A promising membrane material for fuel cells, Renew. Sustain. Energy Rev. 82 (2018) 714–733.
[27] J. Liu, H.J. Choi, L.-Y. Meng, A review of approaches for the design of high-performance metal/graphene electrocatalysts for fuel cell applications, J. Indust. Eng. Chem. 64 (2018) 1–15.
[28] R. Re, et al., Antioxidant activity applying an improved ABTS radical cation decolorization assay, Free Radic. Biol. Med. 26 (1999) 1231–1237.
[29] O.V. Mikolaichuk, et al., Study of biocompatibility, cytotoxic activity in vitro of a tetrazole-containing derivative of 2-amino-4,6-di(aziridin-1-yl)-1,3,5-triazine, Biochem. Biophys. Res. Commun. 629 (2022) 176–182.
[30] V.V. Sharoyko, et al., Biocompatibility, antioxidant activity and collagen photoprotection properties of C60 fullerene adduct with L-methionine, Nanomedicine 40 (2022) 102500.
[31] V.V. Sharoyko, et al., Novel non-covalent conjugate based on graphene oxide and alkylating agent from 1,3,5-triazine class, J. Mol. Liq. 372 (2023) 121203.
[32] L.V. Galebskaya, et al., The importance of a photosensitizer bleaching registration for the evaluation of mechanism of preparation action on the photo-induced hemolysis, Biomed. Photon. 6 (2017) 33–38.
[33] E.I. Pochkaeva, et al., Isothermal calorimetric titration of human serum albumin with the fullerene $C_{60}$-L-arginine adduct, Russ. J. Gen. Chem. 89 (2019) 1731–1733.
[34] I. Herrera, M.A. Winnik, Differential binding models for isothermal titration calorimetry: moving beyond the wiseman isotherm, J. Phys. Chem. B 117 (2013) 8659–8672.
[35] I.N. Gaponenko, et al., Biological evaluation and molecular dynamics simulation of water-soluble fullerene derivative $C_{60}[C(COOH)_2]_3$, Toxicol. Vitro 62 (2020) 104683.
[36] V.V. Sharoyko, et al., Synthesis, characterization and biocompatibility of glycine modified graphene oxide, Fullerenes, Nanotubes and Carbon Nanostructures (2023) 1–12, https://doi.org/10.1080/1536383X.2023.2279550.
[37] P.L. Olive, J.P. Banáth, R.E. Durand, Heterogeneity in radiation-induced DNA damage and repair in tumor and normal cells measured using the 'comet' assay, Radiat. Res. 122 (1990) 86–94.
[38] A.L. Shaw, et al., ATP-competitive and allosteric inhibitors induce differential conformational changes at the autoinhibitory interface of Akt1, Structure 31 (2023) 343–354.e3.
[39] G. Madhavi Sastry, M. Adzhigirey, T. Day, R. Annabhimoju, W. Sherman, Protein and ligand preparation: Parameters, protocols, and influence on virtual screening enrichments, J. Comput. Aided Mol. Des. 27 (2013) 221–234.
[40] M.P. Jacobson, R.A. Friesner, Z. Xiang, B. Honig, On the role of the crystal environment in determining protein side-chain conformations, J. Mol. Biol. 320 (2002) 597–608.
[41] M.P. Jacobson, et al., A hierarchical approach to all-atom protein loop prediction, Proteins: Structure, Function, and Bioinformatics 55 (2004) 351–367.
[42] J.R. Greenwood, D. Calkins, A.P. Sullivan, J.C. Shelley, Towards the comprehensive, rapid, and accurate prediction of the favorable tautomeric states of drug-like molecules in aqueous solution, J. Comput. Aided Mol. Des. 24 (2010) 591–604.
[43] J.D. Thompson, T. Gibson, J.D.G. Higgins, Multiple sequence alignment using clustalw and clustalX, Curr. Protoc. Bioinform. 00 (2003) 2.3.1–2.3.22.
[44] S. Jana, S.K. Singh, Identification of selective MMP-9 inhibitors through multiple e-pharmacophore, ligand-based pharmacophore, molecular docking, and density functional theory approaches, J. Biomol. Struct. Dyn. 37 (2019) 944–965.
[45] C. Lu, et al., OPLS4: Improving force field accuracy on challenging regimes of chemical space, J. Chem. Theory Comput. 17 (2021) 4291–4300.
[46] T.A. Halgren Glide, et al., A new approach for rapid, accurate docking and scoring. 2. enrichment factors in database screening, J. Med. Chem. 47 (2004) 1750–1759.
[47] R.A. Friesner, et al., Extra precision glide: Docking and scoring incorporating a model of hydrophobic enclosure for protein-ligand complexes, J. Med. Chem. 49 (2006) 6177–6196.
[48] Bowers, K. J. *et al.* Scalable Algorithms for Molecular Dynamics Simulations on Commodity Clusters. in *ACM/IEEE SC 2006 Conference (SC'06)* 43–43 (IEEE, 2006). doi:10.1109/SC.2006.54.
[49] W.L. Jorgensen, J. Chandrasekhar, J.D. Madura, R.W. Impey, M.L. Klein, Comparison of simple potential functions for simulating liquid water, J. Chem. Phys. 79 (1983) 926–935.
[50] S. Nosé, A unified formulation of the constant temperature molecular dynamics methods, J. Chem. Phys. 81 (1984) 511–519.
[51] P.A. Greenidge, C. Kramer, J.C. Mozziconacci, R.M. Wolf, MM/GBSA binding energy prediction on the PDBbind data set: Successes, failures, and directions for further improvement, J. Chem. Inf. Model 53 (2013) 201–209.
[52] P.D. Lyne, M.L. Lamb, J.C. Saeh, Accurate prediction of the relative potencies of members of a series of kinase inhibitors using molecular docking and MM-GBSA scoring, J. Med. Chem. 49 (2006) 4805–4808.
[53] C.N. Manners, D.W. Payling, D.A. Smith, Distribution coefficient, a convenient term for the relation of predictable physico-chemical properties to metabolic processes, Xenobiotica 18 (1988) 331–350.
[54] A.A. Meshcheriakov, et al., Physicochemical properties, biological activity and biocompatibility of water-soluble C60-Hyp adduct, Colloids Surf. B Biointerf. 196 (2020) 111338.
[55] Z.R. Huang, S.C. Hua, Y.L. Yang, J.Y. Fang, Development and evaluation of lipid nanoparticles for camptothecin delivery: a comparison of solid lipid nanoparticles, nanostructured lipid carriers, and lipid emulsion, Acta Pharmacol. Sin. 29 (2008) 1094–1102.
[56] K. Ghosh, S. Rathi, D. Arora, Fluorescence spectral studies on interaction of fluorescent probes with Bovine Serum Albumin (BSA), J. Lumin. 175 (2016) 135–140.
[57] M.A. Rashid, S.N. Islam Rabbi, Fluorescence spectroscopic study of interaction between olanzapine and bovine serum albumin, Pharm. Anal. Acta 2015 (2015).
[58] N. Sandu, C.G. Chilom, M. David, M. Florescu, Evaluation of the interaction of levothyroxine with bovine serum albumin using spectroscopic and molecular docking studies 40 (2020) 1139–1151, https://doi.org/10.1080/07391102.2020.1822919.
[59] S.P. Watson, J.M. Auger, O.J.T. McCarty, A.C. Pearce, GPVI and integrin αIIbβ3 signaling in platelets, J. Thrombosis Haemostasis 3 (2005) 1752–1762.
[60] P. Lee, X. Wu, Review: modifications of human serum albumin and their binding effect, Curr. Pharm. Des. 21 (2015) 1862–1865.
[61] D.Y. Lando, et al., Comparative thermal and thermodynamic study of DNA chemically modified with antitumor drug cisplatin and its inactive analog transplatin, J. Inorg. Biochem. 137 (2014) 85–93.
[62] L.F. Leandro, et al., Assessment of the genotoxicity and antigenotoxicity of (+)-usnic acid in V79 cells and Swiss mice by the micronucleus and comet assays, Mutat. Res. 753 (2013) 101–106.
[63] I.A. Prokopiev, E.V. Filippov, G.V. Filippova, N.P. Gladkina, Genotoxicity of usnic-acid enantiomers in vitro in human peripheral-blood lymphocytes, Cell Tissue Biol. 11 (2017) 141–146.
[64] I. Prokopiev, et al., Genotoxicity of (+) and (−)-usnic acid in mice, Mutation Research/genetic Toxicology and Environmental Mutagenesis 839 (2019) 36–39.
[65] M. Song, A.M. Bode, Z. Dong, M.H. Lee, AKT as a therapeutic target for cancer, Cancer Res. 79 (2019) 1019–1031.
[66] P.J. Tsai, Akt: a key transducer in cancer, *J. Biomed. Sci.* 29 (1) (2022) 1–17.
[67] F. Martorana, et al., AKT Inhibitors: new weapons in the fight against breast cancer? Front. Pharmacol. 12 (2021) 662232.
[68] F. Fratev, et al., Discovery of new AKT1 inhibitors by combination of in silico structure based virtual screening approaches and biological evaluations, J. Biomol. Struct. Dyn. 39 (2021) 368–377.
[69] P.J. Trejo-Soto, A. Hernández-Campos, A. Romo-Mancillas, J.L. Medina-Franco, R. Castillo, In search of AKT kinase inhibitors as anticancer agents: structure-based design, docking, and molecular dynamics studies of 2,4,6-trisubstituted pyridines, J. Biomol. Struct. Dyn. 36 (2018) 423–442.
[70] L. Ioakimidis, L. Thoukydidis, A. Mirza, S. Naeem, J. Reynisson, Benchmarking the reliability of qikprop. correlation between experimental and predicted values, QSAR Comb. Sci. 27 (2008) 445–456.
[71] S.A. Hollingsworth, R.O. Dror, Molecular dynamics simulation for all, Neuron 99 (2018) 1129–1143.